https://doi.org/10.5194/egusphere-2026-5697
Preprint. Discussion started: 15 October 2026
© Author(s) 2026. CC BY 4.0 License.

A global description of the three-dimensional structure of temperature anomalies during heat extremes

Hiu-Wang Lau[1], Belinda Hotz[1], Heini Wernli[1], and Robin Noyelle[1]
[1]Institute for Atmospheric and Climate Science, ETH Zürich, Zürich, Switzerland
Correspondence: Hiu-Wang Lau (hiuwang.lau@usys.ethz.ch)

Abstract.

Studying the spatial extent of heat extremes is essential to understand their impacts and physical mechanisms. Although some studies have examined the structure and extent of heat extremes at the surface, few have quantified their horizontal and vertical spatial extent and analyzed their variations with characteristics of heatwaves such as intensity and location. Here, we propose a global and systematic description of the three-dimensional structure of temperature anomalies during surface heat extremes using ERA5 reanalysis data. This is achieved by performing a percentile-based contour-stacking algorithm on the daily mean temperature anomaly field to obtain a representation of the three-dimensional structure of temperature anomalies in the troposphere. We characterize this structure in terms of area, intensity and geometry. We find that near-surface heat extremes have a relatively uniform average area globally, corresponding to the area covered by a circle with a radius of 800 km, although with important geographical variations. The intensity and area of temperature anomalies decrease with height, but much faster in the tropics than in the extratropics. The shape of temperature anomalies at all levels is not circular and is better described by an ellipse with an axis ratio of 0.5–0.6. These ellipses have a systematic preferential orientation that depends mostly on latitude and topography. Tropical temperature anomalies are zonally oriented, but the orientation leans poleward towards higher latitudes, following the direction of anticyclonic wave breaking. Although there is a robust positive correlation between the intensity and the spatial extent of heat extremes in the mid-troposphere, this relationship is more complex and weaker at the surface. We finally advocate against the image of a "heat dome" to describe the vertical structure of temperature anomalies associated to surface heat extremes.

1 Introduction

One of the main consequences of the on-going anthropogenic global warming is the near-ubiquitous increase in the intensity and frequency of extreme heat events (Seneviratne et al., 2021). As a consequence, significant efforts have been made to better understand the physical mechanisms that lead to surface heat extremes (Barriopedro et al., 2023; Domeisen et al., 2023), especially in the mid-latitudes. Generally, temperature anomalies arise from three categories of physical processes (Röthlisberger and Papritz, 2023): advection from climatologically warmer or colder regions, adiabatic warming or cooling by vertical motions, and diabatic changes of (potential) temperature via various processes such as turbulent surface heat fluxes, radiation and latent heat release from water vapor condensation. There are significant regional differences in the contribution

https://doi.org/10.5194/egusphere-2026-5697
Preprint. Discussion started: 15 October 2026
© Author(s) 2026. CC BY 4.0 License.

of these processes to surface heat extremes (Röthlisberger and Papritz, 2023; Mayer, 2025), especially between climatological zones and between land and oceans. From an Eulerian point of view, surface heat extremes in the mid-latitudes arise mainly as a result of the synoptic circulation: strong anticyclones in the mid- to upper-troposphere favor subsidence and clear skies, leading to enhanced surface heating (Barriopedro et al., 2023). Elucidating the physical mechanisms explaining the formation, persistence and/or recurrence of upper-level anticyclones in conjunction with surface heatwaves remains an active area of research (Kornhuber et al., 2017; Röthlisberger et al., 2019; Zschenderlein et al., 2020; Lembo et al., 2024). The dynamics of Rossby waves (Wicker et al., 2024) and their interaction with large-scale topography (Jiménez-Esteve et al., 2022; Jiménez-Esteve and Domeisen, 2022; Tan et al., 2024) has been outlined as a key mechanism for explaining upper-level synoptic dynamics during heatwaves. Land-atmosphere coupling also plays a central role in the intensification of heat extremes, through soil desiccation and the partition of energy fluxes from latent to sensible heat fluxes in the boundary layer (Seneviratne et al., 2010; Wehrli et al., 2019; Miralles et al., 2019). More localized heat extremes can also be formed under the influence of large-scale topography through adiabatic warming of downward-moving air masses through foehn effects (Elvidge and Renfrew, 2016; McGregor, 2024).

In polar regions, upper-level anticyclones are also prevalent during heat extremes (Papritz, 2020), but case studies have shown that advection of warm and moist air likely plays the major role in eroding the climatological near-surface temperature inversion (Blanchard-Wrigglesworth et al., 2023; Wille et al., 2024). Finally, in equatorial regions, heat extremes occur when moist convection is suppressed, because of reduced soil moisture and humidity in or dry air entrainment above the boundary layer (Joshi et al., 2008; Byrne, 2021; Zhang et al., 2021; Costa et al., 2022; Duan et al., 2024). In the subtropics, heat extremes can also be induced at the synoptic scale by approaching tropical cyclones along coastal areas, where peripheral downdrafts suppress convection, leading to strong radiative heat fluxes and promoting adiabatic heating through air subsidence (Zhang et al., 2024).

Despite substantial, systematic and global investigations of the processes leading to surface heat extremes, there have been much fewer investigations of the entire vertical structure of the atmosphere during these extremes. This comes as a surprise given that (i) the physical mechanisms occurring on the vertical dimension are fundamental to the coupling between the synoptic dynamics and the surface extremes (O'Gorman and Schneider, 2009; Zhang and Boos, 2023), and (ii) there are indications of substantial vertical variability in these mechanisms (Zschenderlein et al., 2020; Neal et al., 2022; Schumacher et al., 2022; Oertel et al., 2023; Hotz et al., 2024). Recent studies have hypothesized that the vertical structure of temperature may be important to explain the intensity of very intense extremes (Zhang and Boos, 2023; Nicolas and Hotz, 2026). Miralles et al. (2014) showed, for two case studies of very intense heatwaves, that the vertical dimension can act as a heat storage during the night, which re-enters the BL during the day. Brunner et al. (2016), Brunner and Steiner (2017) and Nabizadeh et al. (2021) found vertically deep positive temperature anomalies inside summer anticyclones associated with heatwaves, similar to model results (Noyelle et al., 2025). Zhang and Boos (2023) put light on the importance of the vertical dimension for heat extremes by proposing that, similar to the tropics, the surface intensity of mid-latitude heat extremes is constrained by moist convection and upper-level environmental conditions. This ignited interest in evaluating the merits and limits of this approach for understanding and constraining surface heat extremes (Duan et al., 2024; Li and Tamarin-Brodsky, 2026; Nicolas and Hotz, 2026; Noyelle

https://doi.org/10.5194/egusphere-2026-5697
Preprint. Discussion started: 15 October 2026
© Author(s) 2026. CC BY 4.0 License.

et al., 2026). Using a Lagrangian approach on three case studies of record-breaking events, Hotz et al. (2024) found vertically deep temperature anomalies but with varying importance of associated physical mechanisms from one event to another. Lhotka and Kyselý (2024) investigated systematically European atmospheric heat extremes based on whether they occur at the surface, in the mid-troposphere, in the high-troposphere or throughout the vertical profile. Subsequent works used the same approach to investigate the link between heatwaves at different levels and the atmospheric circulation (Poppová et al., 2026) and evaluate regional models (Plavcová et al., 2025). Hotz et al. (2026) is the only global study to have looked systematically and globally at the vertical profile of temperature anomalies during surface heat extremes, showing that the vertical profiles cluster into three climatological zones (polar, mid-latitude and equatorial regions) corresponding to distinct shapes of the temperature anomalies profiles. However, this study also did not consider the horizontal dimension of heat extremes.

A few studies have proposed methods to quantify the horizontal extent of heat extremes and their spatial or temporal variations (Lyon et al., 2019; Cebrián et al., 2022; Luo et al., 2022; Happé et al., 2024), although they are often confined to the surface or take into account the vertical dimension only through one mid- or upper vertical level (usually at 500 hPa). As a consequence, most of what is known about the three-dimensional, i.e., combined vertical and horizontal, structure of temperature anomalies during heat extremes is based so far on case studies only.

This study aims to systematically and globally describe the three-dimensional structure of temperature anomalies during surface heat extremes and quantify their size and geometry. In particular, we address the following three questions:

1. What are the typical area, shape and orientation of temperature anomalies across the troposphere during surface heat extremes?
2. How do these characteristics vary geographically?
3. How do these characteristics relate to the intensity of surface heat extremes?

The paper is organized as follows. In Sect. 2 we detail the data used, the computation of the temperature anomalies, and the detection and stacking algorithm. In Sect. 3 we present the results obtained. The results and the limitations of the algorithm are discussed in Sect. 4. Finally, we present the conclusions reached in Sect. 5.

2 Data and methods

2.1 Reanalysis data and temperature anomaly computation

Throughout the paper, we use the three-dimensional (3D) temperature data from the ERA5 global reanalyses from the European Centre for Medium-Range Weather Forecasts (ECMWF) over the period 1951-2023 (Soci et al., 2024). We use 3D daily mean temperature and surface daily maximum temperature with a 0.5 degree resolution horizontally. Vertically, we select all data from hybrid sigma-pressure levels $\{k \,|\, 137 \geq k \geq 80\}$, which correspond to pressure levels between approximately 1000 hPa and 260 hPa, covering most of the troposphere. For simplicity, we call them "model levels" in the following. All computations are first performed on model levels and then converted to pressure using 1000 hPa as a surface pressure reference. This choice

https://doi.org/10.5194/egusphere-2026-5697
Preprint. Discussion started: 15 October 2026
© Author(s) 2026. CC BY 4.0 License.

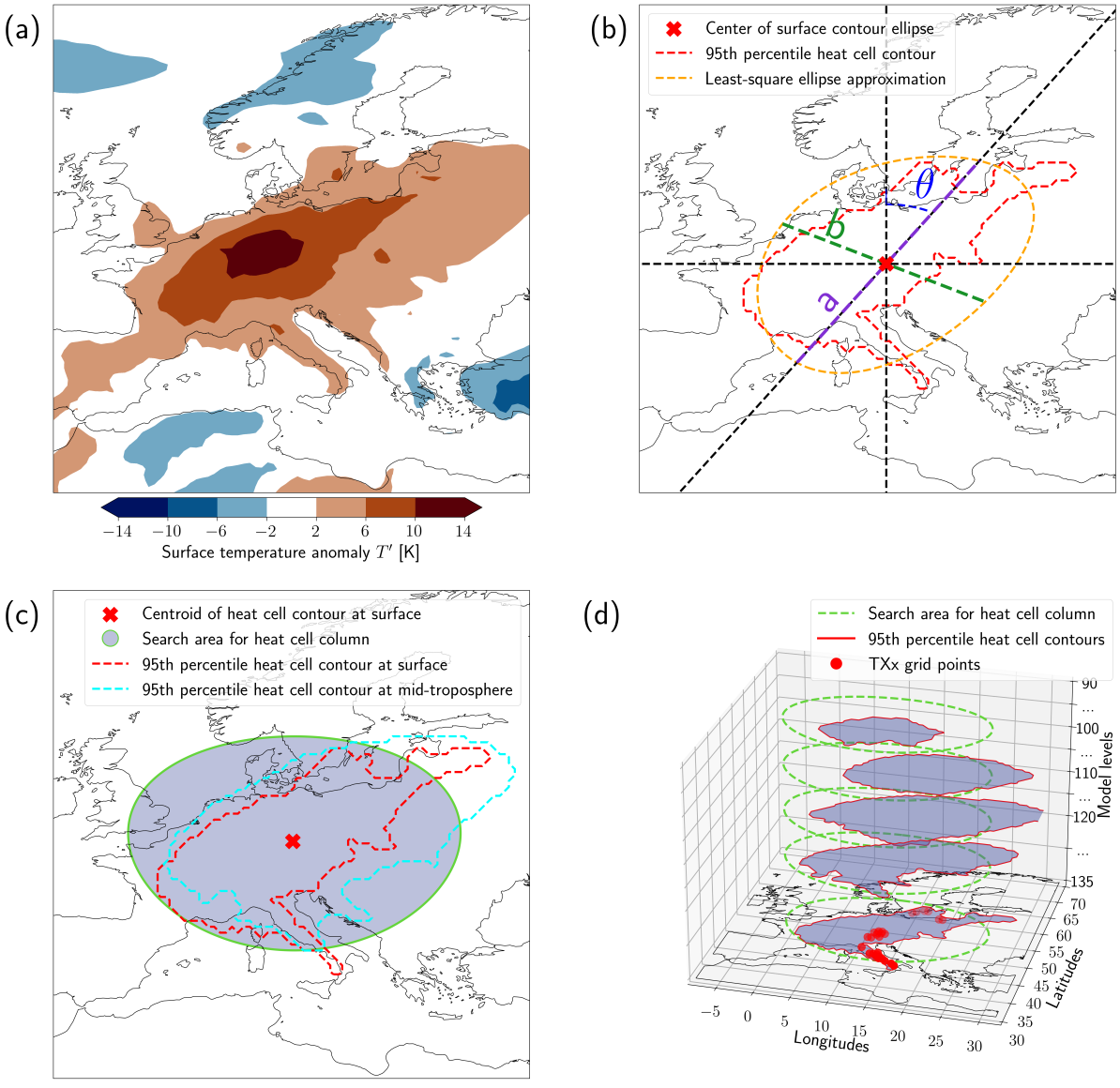


Figure 1. Example of the heat cell identification procedure for a heat extreme event on 28 August 1964 over Central Europe. **(a)** Daily mean temperature anomaly T' at the lowest model level. **(b)** Corresponding 95th percentile contour (red), defining the surface "heat cell", least-square fit of an ellipse (orange) on the heat cell contour and corresponding shape parameters: semi-major axis a, semi-minor axis b, and orientation angle θ with respect to the hemispheric pole. **(c)** Associated mid-tropospheric heat cell contour (light-blue) overlapping with the search area (shaded), centered at the centroid (red dot) of the surface heat cell (red). **(d)** 3D schematic of the heat cell contour stack produced by the stacking algorithm, with the red dots denoting surface grid points experiencing a TXx event. Only 5 levels are shown for illustration.

https://doi.org/10.5194/egusphere-2026-5697
Preprint. Discussion started: 15 October 2026
© Author(s) 2026. CC BY 4.0 License.

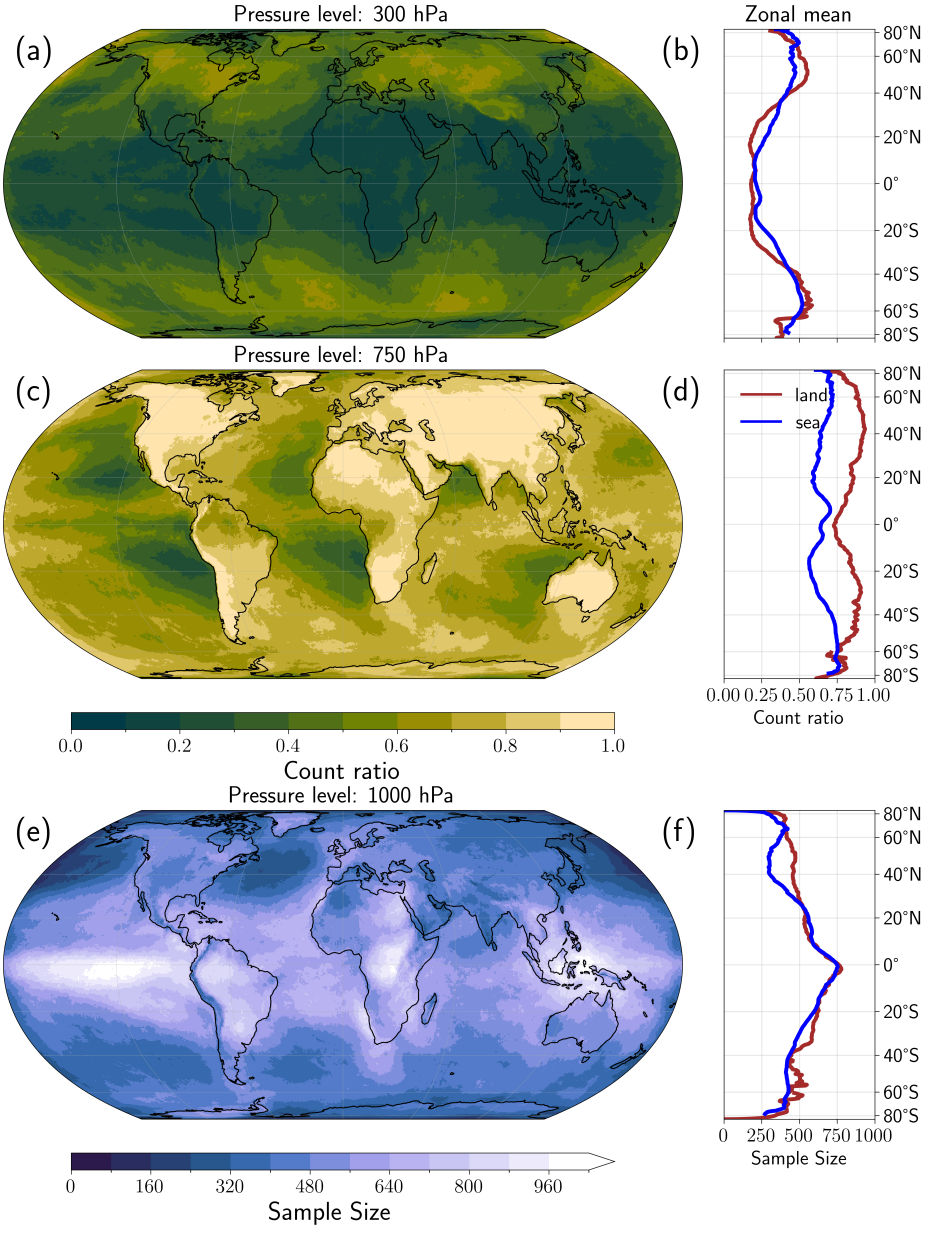


Figure 2. Vertical distribution of the number of identified heat cells. Fraction of the number of heat cells with respect to the surface heat cell sample size at **(a)** 300 hPa and **(c)** 750 hPa. **(b, d)** Corresponding zonal means for land and sea grid points. **(e)** Total sample size of the surface heat cells and **(f)** its zonal mean.

was made for visualization purposes. In the following, we group the vertical levels into lower (1000–900 hPa), mid- (750–550 hPa) and upper troposphere (400–300 hPa) using this reference pressure. This is done using a fixed range of model levels

https://doi.org/10.5194/egusphere-2026-5697
Preprint. Discussion started: 15 October 2026
© Author(s) 2026. CC BY 4.0 License.

for each category, and the corresponding pressure range thus reflects a typical range for ocean grid points. For high elevation grid points, these ranges of pressure do not represent the actual range of pressures.

Temperature anomalies are computed analogously to Röthlisberger and Papritz (2023). We first compute a moving climatology T_{clim} as the average of the daily mean temperatures over a centered window of 21 days and 9 years at each day, grid point (i, j), and vertical level k. We then obtain the temperature anomaly T' as the difference with the absolute temperature:

$$T'(i,j,k) = T(i,j,k) - T_{clim}(i,j,k). \tag{1}$$

This computation of the temperature anomalies is assumed to remove both the seasonal cycle and the long-term drift due to anthropogenic global warming.

The ERA5 data set tends to underestimate near-surface maximum temperatures and thus introduces potential bias in the quantification of the intensity of heat extremes at the surface (Lopes et al., 2024). Given that we work mainly with daily-average temperature fields and that ERA5 is known to have good performance in representing atmospheric features at synoptic scales, i.e., at the scales of typical heat extremes (Soci et al., 2024), this bias should not impact our analyses. We thus consider that ERA5 well represents the temperature anomaly field during heat extremes in the following.

2.2 Finding vertical temperature anomaly stacks

To obtain a representation of the 3D temperature anomalies associated with a surface heat extreme, we start with the lowest model level. We consider a grid point to be part of a heat extreme if its daily mean temperature anomaly is higher than the local 95th climatological quantile. For each grid point (i, j), vertical level k, and day of the year, we estimate the 95th climatological quantile T'_{q95} of the distribution of temperature anomalies T' within a 21-day-of-year centered window and across all years considered (1951-2023), i.e. 1533 data points.

We use the marching square algorithm (Maple, 2003) from Python's ContourPy library to generate contours that enclose the area formed from grid points that are part of a heat extreme (i.e., with T' above the 95th quantile). This contour is represented by a series of n coordinate vertices of the grid: $\{(\lambda_i, \varphi_i)\}_{i=1}^{n}$ where λ stands for longitude and φ for latitude. We call the contiguous area formed from the collection of heat extreme grid points a "heat cell". The boundary of this area — i.e. the polygon $\{(\lambda_i, \varphi_i)\}_{i=1}^{n}$ — is called a "heat cell contour". To handle contours crossing the International Date Line, the computation is done on a longitudinally-extended global grid such that the longitude values stay continuous at the date line.

We proceed to implement a number of criteria to filter surface heat cell contours. First, we impose that every heat cell contour should be a closed contour on the Earth's surface by checking that the starting coordinate vertex is the same as the ending coordinate vertex (i.e. $\lambda_1 = \lambda_n$ and $\varphi_1 = \varphi_n$). Second, we check whether a heat cell contains at least one grid point with an annual maximum 2-meter temperature (TXx) event that occurs on the same day. This is done to ensure that we do not select extremes in the cold season. In addition, we impose a minimum and maximum heat cell area to constrain the physical scales of the heat cells, see below for how we compute the area of a heat cell. We discard heat cells that have an area $\mathcal{A}$ below $\mathcal{A}_{min} = 31415\,\mathrm{km}^2$ (equivalent radius of $r_{\mathcal{A}} = 100\,\mathrm{km}$, see below) or above $\mathcal{A}_{max} = 1.9 \times 10^7\,\mathrm{km}^2$ (equivalent radius

https://doi.org/10.5194/egusphere-2026-5697
Preprint. Discussion started: 15 October 2026
© Author(s) 2026. CC BY 4.0 License.

of $r_{\mathcal{A}} = 2500\,\mathrm{km}$) in order to filter out highly localized temperature anomaly spikes and large-scale atmospheric systems that generate large regions of positive temperature anomalies that are not associated with surface heat extremes. The choice of the minimum and maximum area values is discussed in Sect. 4 and does not impact our results in any major way. Figure 1a shows an example of a surface temperature anomaly map over Europe, and Fig. 1b shows the corresponding heat cell contour at the surface.

Once heat cells have been identified on the lowest model level, we proceed to search for the vertical temperature anomaly structure. We use temperature anomaly fields at the other model levels to find heat cells above the surface. We then stack heat cells that are considered to be part of the same heat extreme together. We call such a vertical ensemble of heat cells a "heat cell stack". The stacking algorithm proceeds as follows:

- **Step 1:** We consider the centroid $\mathbf{c}$ of the surface heat cell contour, defined as:

$$\mathbf{c} := (\lambda_c, \varphi_c) = \left(\frac{1}{n} \sum_{i=1}^{n} \lambda_i,\ \frac{1}{n} \sum_{i=1}^{n} \varphi_i \right). \tag{2}$$

  We define a search area with a 500 km radius (hereby named R_{search}) around this centroid (shaded geodesic circle with green perimeter in Fig. 1c) to be used for the search of heat cell contours at the vertical levels above. The computations are also done on a longitudinally-extended grid to handle centroid calculation of contours crossing the International Date Line.

- **Step 2:** For each model level k, we search for heat cell contours similarly to the lowest model level. At each vertical level, a heat cell contour is considered to be associated with the same heat extreme as the surface heat cell contour if it is found to overlap with the search area defined around the centroid, i.e. when the heat cell contour has at least one grid point that is inside the search area. An example of this overlap is illustrated in Fig. 1c, where the cyan contour overlaps the search area centered at the centroid of the surface contour (red contour). The reason for defining a search area instead of directly checking for contour overlaps is discussed in Sect. 4.

- **Step 3:** We group all the heat cell contours found at each vertical level together with the original surface heat cell contour to form a "heat cell contour stack" (Fig. 1d). This resulting contour stack is therefore the discretized representation of the 3D volume of temperature anomalies associated with a surface heat extreme.

Intense and persistent heat extremes are more likely to be associated with barotropic anticyclones (Wang et al., 2022; Jin et al., 2024; Vakrat and Kushner, 2025; Noyelle et al., 2025) for which the vertical tilt of the temperature anomaly structure is relatively small. Therefore, heat cell stacks are likely to have a vertically continuous structure. We are thus confident in the assumption that the overlap check can select the heat cell contour at each vertical level that belongs to the same heat extreme as the one on the lowest model level. Previous work (Hotz et al., 2026) also showed that temperature anomalies during heat extremes extend vertically at the same grid point. Repeating the above operation for every surface heat cell contour between

https://doi.org/10.5194/egusphere-2026-5697
Preprint. Discussion started: 15 October 2026
© Author(s) 2026. CC BY 4.0 License.

1951 and 2023, we obtain a collection of heat cell stacks associated with surface heat extremes during this period. Note that we do not consider the temporal dimension here, therefore a heat extreme lasting several days is considered as independent heat cell stacks.

The implementation of the heat cell selection criteria and the event-specific nature of the stacking algorithm implies that (i) there is not a constant number of heat cell stacks per grid point (Fig. 2e) and (ii) not every surface heat extreme is associated with a temperature anomaly structure that extends throughout the troposphere (Fig. 2a–d). The TXx event association criterion limits the sample size of every grid point by ensuring that every sample is associated with at least one TXx event in the vicinity, which leads to different sample sizes at the surface. There are generally more surface heat cell instances in the tropics compared to the middle and high latitudes (Fig. 2e), likely due to differences in the average area of heat cells as seen later in Sect. 3. Vertically, since heat extremes are of surface origin and the temperature anomalies are larger close to the surface (Hotz et al., 2026), we expect the sample size of heat cells to decrease at subsequent vertical levels, with the rate of decrease depending on the average vertical extent of the heat extremes in the region. While over mid-latitudes land, this decrease at $300\,\mathrm{hPa}$ corresponds to 50% of the surface sample size, in the tropics it can decrease down to 25% (Fig. 2a).

The decrease in heat cell sample size introduces missing data points within our datasets, mostly at vertical levels above the vertical extent of a heat cell stack. Since the calculation of heat cell metrics (see below) is based on the presence of a heat cell, when no heat cell is detected at a vertical level, the corresponding metric is not considered in the calculation of the corresponding mean value. This results in the statistics of the metrics considered being biased towards taller heat cell stacks, especially at upper levels. As shown in Sect. 3.3, these events likely correspond to surface heat extremes with higher intensities. Thus, one should keep in mind this inherent statistical bias when interpreting the results of heat cell characteristics. An exception from this bias is the heat cell area, which is counted as zero when no heat cell is found.

2.3 Definition of heat cell area and geometry

From the collection of heat cell contour stacks, we extract several metrics to represent the 3D structure of temperature anomalies during surface heat extremes. First, we quantify the spatial extent of each heat cell in the contour stack as the geodesic area of the heat cell. The geodesic area $\mathcal{A}$ is defined as the surface integral:

$$\mathcal{A} = \iint_{\Omega} \mathrm{d}S, \tag{3}$$

where Ω denotes the region enclosed by the heat cell contour on the Earth's surface. In practice, the area is computed using Python Pyproj's algorithm (Evenden et al., 2026), where the geodesic area of an input polygon (i.e., the heat cell contour) is computed over the World Geodetic System 1984 (WGS84) ellipsoid (Kumar, 1988). This area can be expressed in km^2, but for a more intuitive comparison, we define a first-order circle approximation to the contour and express the area $\mathcal{A}$ in terms of the equivalent radius that a circle with the same area would have:

$$r_{\mathcal{A}} := \sqrt{\frac{\mathcal{A}}{\pi}}, \tag{4}$$

where $r_{\mathcal{A}}$ is expressed in km. At vertical levels where no heat cell is found, the area is set to zero.

https://doi.org/10.5194/egusphere-2026-5697
Preprint. Discussion started: 15 October 2026
© Author(s) 2026. CC BY 4.0 License.



However, as shown in Fig. 1b, actual heat cells do not need to be circular. To quantify the geometric characteristics of heat cells at the second order, we approximate their shape with an ellipse. An ellipse approximation provides additional geometrical parameters, namely orientation angle θ and axis ratio q (see below), in addition to the area of the heat cell. The equation of an ellipse on a Cartesian (x, y) plane can be written as:

$$Ax^2 + Bxy + Cy^2 + Dx + Ey + F = 0, \tag{5}$$

where (A, B, C, D, E, F) are the conic coefficients. We estimate these coefficients via a least-squares ellipse fitting method that minimizes the algebraic residual of the conic equation:

$$(\hat{A}, \hat{B}, \hat{C}, \hat{D}, \hat{E}, \hat{F}) = \underset{(A,B,C,D,E,F)}{\operatorname{argmin}} \sum_{i=1}^{N} \left(Ax_i^2 + Bx_iy_i + Cy_i^2 + Dx_i + Ey_i + F\right)^2, \tag{6}$$

where $\{(x_i, y_i)\}_{i=1}^n \subset \mathbb{R}^2$ is the set of n vertices that represent the heat cell contour in a local Cartesian plane with azimuthal equidistant projection from the set of heat cell longitude-latitude coordinate pairs $\{(\lambda_i, \varphi_i)\}_{i=1}^n$ (see appendix B for the details). The estimated set of conic coefficients parametrizes an ellipse that best fits the original shape and orientation of the heat cell contour. We subsequently obtain three key geometric parameters that summarize the shape of the ellipse: the semi-major axis length a, the semi-minor axis b and the orientation angle θ, see appendix C for a detailed derivation from the estimated $(\hat{A}, \hat{B}, \hat{C}, \hat{D}, \hat{E}, \hat{F})$. These parameters are shown in Fig. 1b for the illustrated case. Note the deformation of the ellipse when projected on a latitude–longitude regular map. The semi-major and semi-minor axes together represent the horizontal dimension of the ellipse and the amount by which it differs from a circle ($a = b$ for a circle). We measure the deviation from the circle approximation using the axis ratio:

$$q = \frac{b}{a}. \tag{7}$$

A q value of 1 therefore represents a circle, with the shape becoming more stretched along the semi-major axis as q approaches 0. Meanwhile, the orientation angle is defined with respect to the direction of the respective poles in the two hemispheres. Therefore, the direction of 0°points north in the northern and south in the southern hemisphere, respectively, see Fig. 1b and Fig. 6 for examples. When averaging orientation angles over several events occurring over the different grid points, we use a circular mean (Mardia and Jupp, 1999) instead of the standard averaging.

It should be noted that there are underlying assumptions made when we re-project the heat cell in a Cartesian coordinate plane that introduce errors in the values of axes lengths and orientation angles. Nevertheless, we find these errors to be minimal (approx. 0.1%) under the typical length scales of the heat events detected (see Appendix B). In addition, the ellipse approximation and the associated geometric parameters are most representative of the original heat cell if the shape of the heat cell is regular. Similarly to what is shown in Fig. 6b, if the shape of a heat cell is irregular and complex, the ellipse will inevitably be a less accurate representation of the original geometry.

https://doi.org/10.5194/egusphere-2026-5697
Preprint. Discussion started: 15 October 2026
© Author(s) 2026. CC BY 4.0 License.

2.4 Heat cell area vs intensity

In addition to quantifying the spatial characteristics of heat extremes, we investigate how the intensity of surface heat extremes is related to their vertical temperature anomaly structure. We compute correlations between heat cell area $\mathcal{A}$ and corresponding intensity at two vertical levels, at model level 137 (approx. 1000 hPa) and model level 97 (approx. 500 hPa), representing respectively the near-surface and free atmosphere. We define the intensity of a heat cell using the temperature anomaly values within the heat cell contour. We use two metrics to measure the intensity of a heat cell: the mean value of the temperature anomalies T' for all grid points within the heat cell contour and the maximum value of temperature anomalies T' within the heat cell contour. For each combination of area and intensity metric, we compute the Spearman rank correlation between the two. We use the Spearman rather than Pearson correlation for its robustness to outliers and its capacity to quantify non-linear relationships. We therefore obtain four correlations between the heat cell area and maximum T' at 500 hPa ($\rho_{\mathcal{A}}(TX_{500})$), mean T' at 500 hPa ($\rho_{\mathcal{A}}(TM_{500})$), maximum T' at 1000 hPa ($\rho_{\mathcal{A}}(TX_s)$) and mean T' at 1000 hPa ($\rho_{\mathcal{A}}(TM_s)$).

3 Results

3.1 Heat cells area and maximum intensity

Globally, surface heat cells have an average equivalent radius $r_{\mathcal{A}}$ of around 800 km (Fig. 3e). This value is almost constant with latitude both over land and oceans when zonally averaged (Fig. 3f), but there are important regional differences. The largest heat cells over land, with an average $r_{\mathcal{A}}$ exceeding 960 km, are found at the center of major continents (Eurasia, Africa, North and South America). Meanwhile, the smallest land-based heat cells at the surface are found close to large-scale mountain ranges such as the Himalayas and the Andes. It is already known from previous work that large-scale topography can affect the location and frequency of heat extreme occurrences through modifications of the temperature structure and large-scale circulations (Jiménez-Esteve and Domeisen, 2022). They therefore also likely influence the area extent of heat cells through similar physical mechanisms. Over the oceans, the largest heat cells are found in the central Pacific region, which very likely reflects ENSO anomalies of SSTs, with $r_{\mathcal{A}}$ above 1120 km. Large heat cells are also found over subtropical highs. The smallest surface heat cells are found both near the North Pole and around the maritime continent. Note that there is substantial spread in the values of $r_{\mathcal{A}}$ for individual heat cells (Fig. A1g-i), with the 90th quantile of the distribution of $r_{\mathcal{A}}$ being up to twice as large as the mean.

Above the surface, the average extent of heat cells gradually decreases with height: in the upper troposphere, the zonally averaged $r_{\mathcal{A}}$ drops to around 200 km for tropical heat cells and just below 400 km for mid- to high-latitude heat cells (Fig. 3b,d). The decrease in area is more intense in the tropics, with the average $r_{\mathcal{A}}$ of some tropical grid points dropping to near-zero in the middle and upper troposphere (Fig. 3a,c). Meanwhile, the average $r_{\mathcal{A}}$ heat cells in the extratropics remain relatively high even at upper levels. The more intense vertical decrease in area extent for heat cells in the tropics indicates that there are, on average, fewer heat extremes that reach the upper levels compared to the extratropics, indicating that tropical heat extremes have a vertical extent confined to the lower levels. This is consistent with the results of Hotz et al. (2026), who showed that

https://doi.org/10.5194/egusphere-2026-5697
Preprint. Discussion started: 15 October 2026
© Author(s) 2026. CC BY 4.0 License.

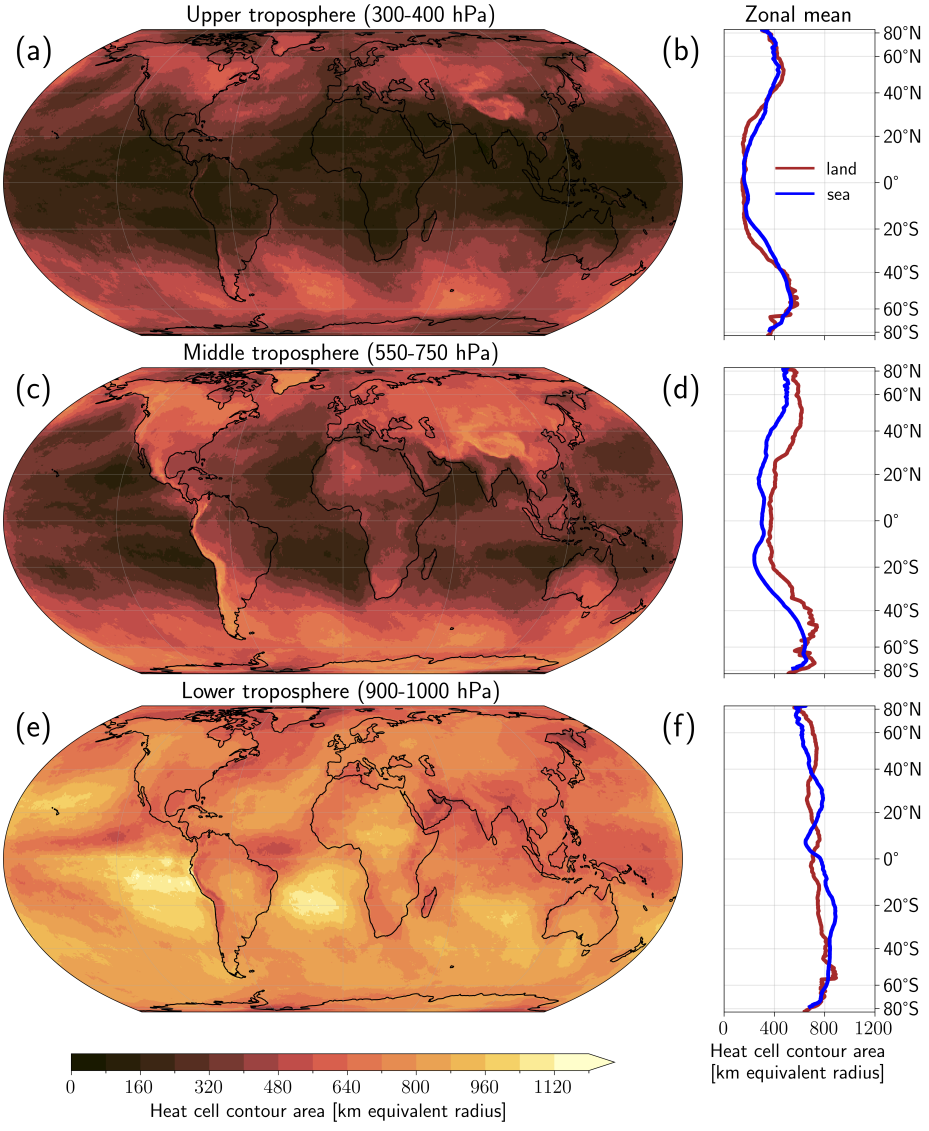


Figure 3. Averaged values of the heat cell equivalent radius $r_{\mathcal{A}}$ (in km) at three vertical layers: **(a, b)** upper troposphere (300–400 hPa), **(c, d)** middle troposphere (550–750 hPa) and (e, f) lower troposphere (900–1000 hPa). **(b, d, f)** show the corresponding zonal means for grid points over land (red) and over ocean (blue).

heat extremes in the tropics are confined mainly to the lower troposphere. It should be noted that the heat cells remaining in the upper levels of the tropics still have a similar range in area as the lower levels if the sample points with zero area extent are ignored (Fig. A1a,d). This shows that the low average $r_{\mathcal{A}}$ at upper levels in the tropics is skewed by the large fraction of samples with zero $r_{\mathcal{A}}$.

https://doi.org/10.5194/egusphere-2026-5697
Preprint. Discussion started: 15 October 2026
© Author(s) 2026. CC BY 4.0 License.

Large-scale topography also influences the area of heat cells in the middle troposphere, creating anomalously large heat cells in regions with high topography such as the Tibetan Plateau (Fig. 3c). In addition, a systematic land-sea contrast is seen for heat cells in the middle troposphere, particularly in the extratropics, where the average $r_{\mathcal{A}}$ of heat cells over land is generally higher than over the ocean (Fig. 3c,d). In the extratropics, in contrast to the tropics, the distribution of heat cell area is more zonally and vertically homogeneous, especially over land. Based on the fact that Rossby waves are known to play an important role in the formation of mid-latitude heat extremes (Jiménez-Esteve and Domeisen, 2022; Domeisen et al., 2023; Barriopedro et al., 2023), we hypothesize that the spatial configuration of Rossby wave packets also plays a role in modulating the area extent of mid-latitude heat cells, making them more zonally consistent in the middle troposphere.

Contrary to the mean area, the maximum intensity of heat cells shows a strong meridional gradient that is preserved from the lower to the upper troposphere (Fig. 4). Anomalies amount to up to 10 K in the mid-latitudes, but only reach 3 K in the tropics. This meridional gradient reflects the climatologically higher variability of temperature anomalies at higher latitudes (Hotz et al., 2026), which is captured here when using a local high quantile to identify heat cells. Land and ocean grid points have similar maximum temperature anomalies in the middle and upper troposphere (Fig. 4b,d), but land extremes are 3–4 K more intense than ocean extremes at the surface (Fig. 4f). The maximum intensity of heat cells decreases with height, but not as much as one could expect based on previous work (Hotz et al., 2026). As discussed in Sect. 4.1, this is likely the results of the bias introduced by filtering events that do not reach a certain level, which favors more intense events. The mean intensity of heat cells show similar patterns as the maximum intensity (Fig. A4).

3.2 Geometry of heat cells

As detailed in Sect. 2.3, we fit an ellipse to individual heat cell contours as an approximation of their shape and analyze their dimensions and orientation. The axis ratio of the heat cell ellipses is remarkably homogeneous throughout the troposphere and across the globe: most of the ellipses have an axis ratio of around 0.5–0.6 (Fig. 5a,c,e), with medians over land and ocean at the surface being 0.57 and 0.51, respectively. This indicates that the length of the semi-minor axis is around half the length of the semi-major axis for most heat cell ellipses, which implies that heat cells are indeed not circular in shape on average, but tend to be stretched in a particular direction. There are also regions with a lower axis ratio, down to 0.3, especially over the ocean at the near-surface level. This occurs particularly over subtropical highs and parts of the equatorial ocean (Fig. 5e). This indicates that heat cells in these regions are more elongated compared to the other regions and likely reflect the shape of underlying SST anomalies. The geographical variability of the axis ratio decreases with height, with the mean axis ratio in the middle and upper troposphere closer to the 0.5–0.6 range. There is also substantial spread in the distribution of the axis ratio for individual heat cells (Fig. A2), however with more similar distributions between regions and levels than for the equivalent radius. Nevertheless, very few heat cells reach an axis ratio between 0.9 and 1 (less than 1%), which indicates that the non-circular shape of heat cells is a robust geometric feature.

As a result of this non-circular shape, one can reliably define the angle θ that measures the orientation of each ellipse with respect to its hemispheric pole. We find a systematic meridional gradient in θ throughout the troposphere: heat cells tend to orient zonally in the tropics and then gradually change to a northeast-southwest orientation in the mid-latitudes of the Northern

https://doi.org/10.5194/egusphere-2026-5697
Preprint. Discussion started: 15 October 2026
© Author(s) 2026. CC BY 4.0 License.

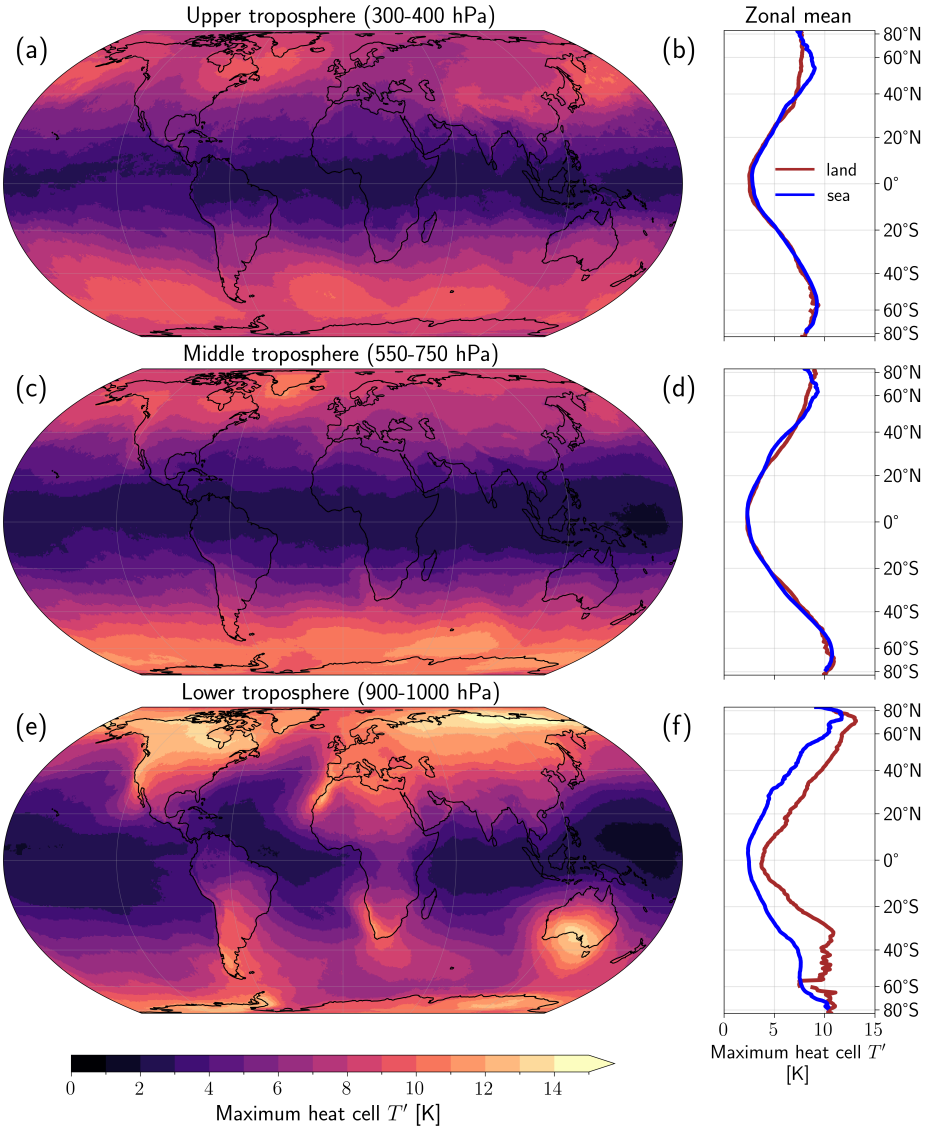


Figure 4. As Fig. 3 for the maximum values of T' in heat cells.

Hemisphere (e.g., Fig. 6b) and a northwest-southeast orientation in the Southern Hemisphere (e.g., Fig. 6g), corresponding to $\theta \simeq 60°$. An example of the zonal orientation near the equator is shown in Fig. 6c,d and of the northwest-southeast orientation in the Southern Hemisphere mid-latitudes in Fig. 6g,h. In the mid-latitudes, this orientation reflects the usual direction of anticyclonic wave breaking (Weijenborg et al., 2012), which is typically associated with the formation of persistent ridges creating the conditions for surface heat extremes (Barriopedro et al., 2023).

https://doi.org/10.5194/egusphere-2026-5697
Preprint. Discussion started: 15 October 2026
© Author(s) 2026. CC BY 4.0 License.

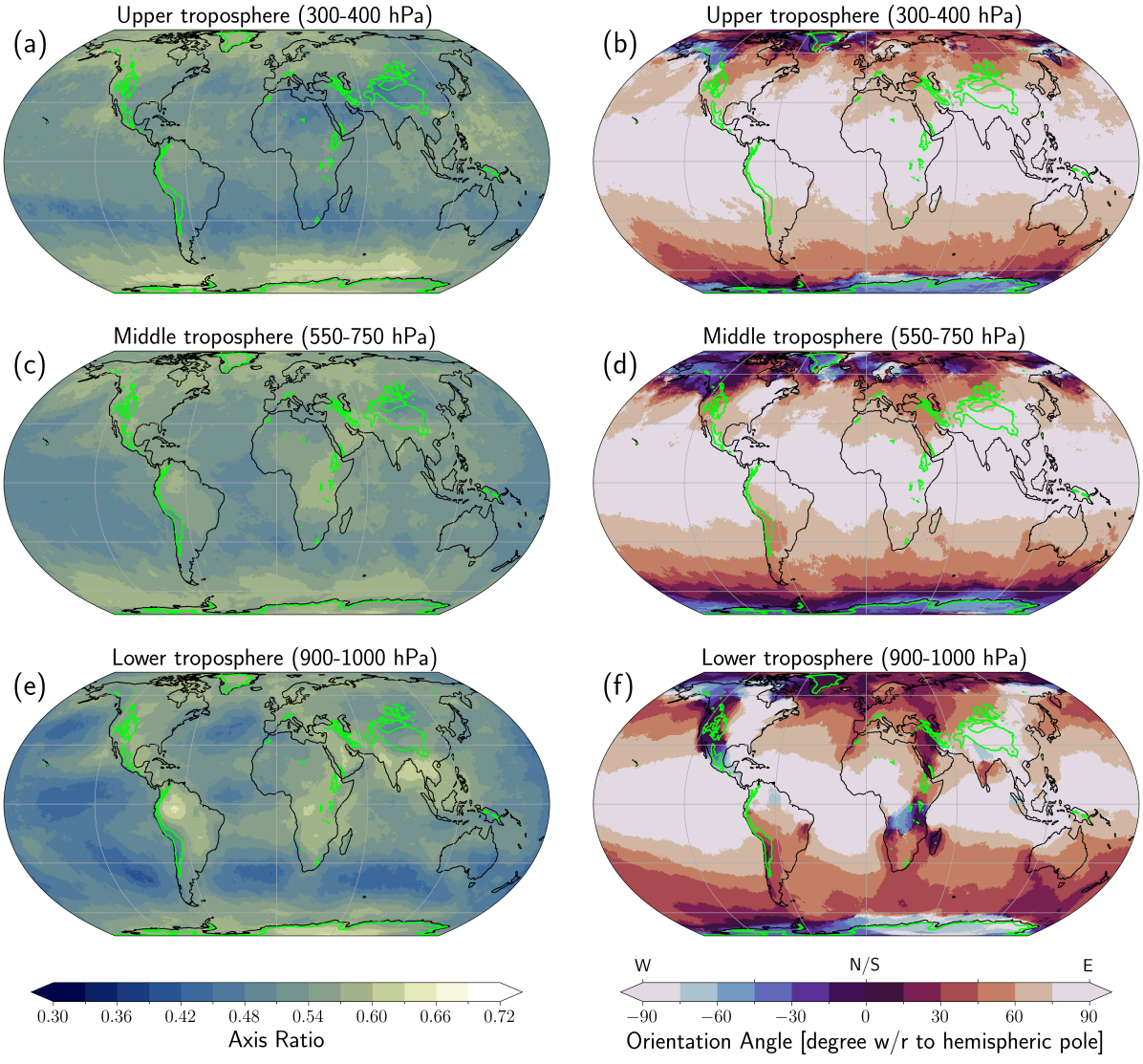


Figure 5. Mean geometry of heat cells. (Left column) Mean axis ratio q and (right column) orientation angle θ at the same vertical layers as in Fig. 3. For the orientation angle θ, the values range from -90 degrees to $+90$ degrees with respect to the respective hemispheric pole. Green contours indicate topographic features above 1750 m.

There is a strong topographic influence on the variation of θ near the surface. The orientation of heat cells near large-scale topographic features tends to follow the orientation of the topography itself: for example the Rocky Mountains in North America, the Andes in South America and the Great Rift Valley of Africa all have orientation angles that are very different than the heat cells at similar latitudes without major surrounding mountains (Fig. 5f). Specific examples of topographic alignment of a surface heat cell can be seen in Fig. 6a,e. A striking feature of the surface orientation angle is the difference between North

https://doi.org/10.5194/egusphere-2026-5697
Preprint. Discussion started: 15 October 2026
© Author(s) 2026. CC BY 4.0 License.

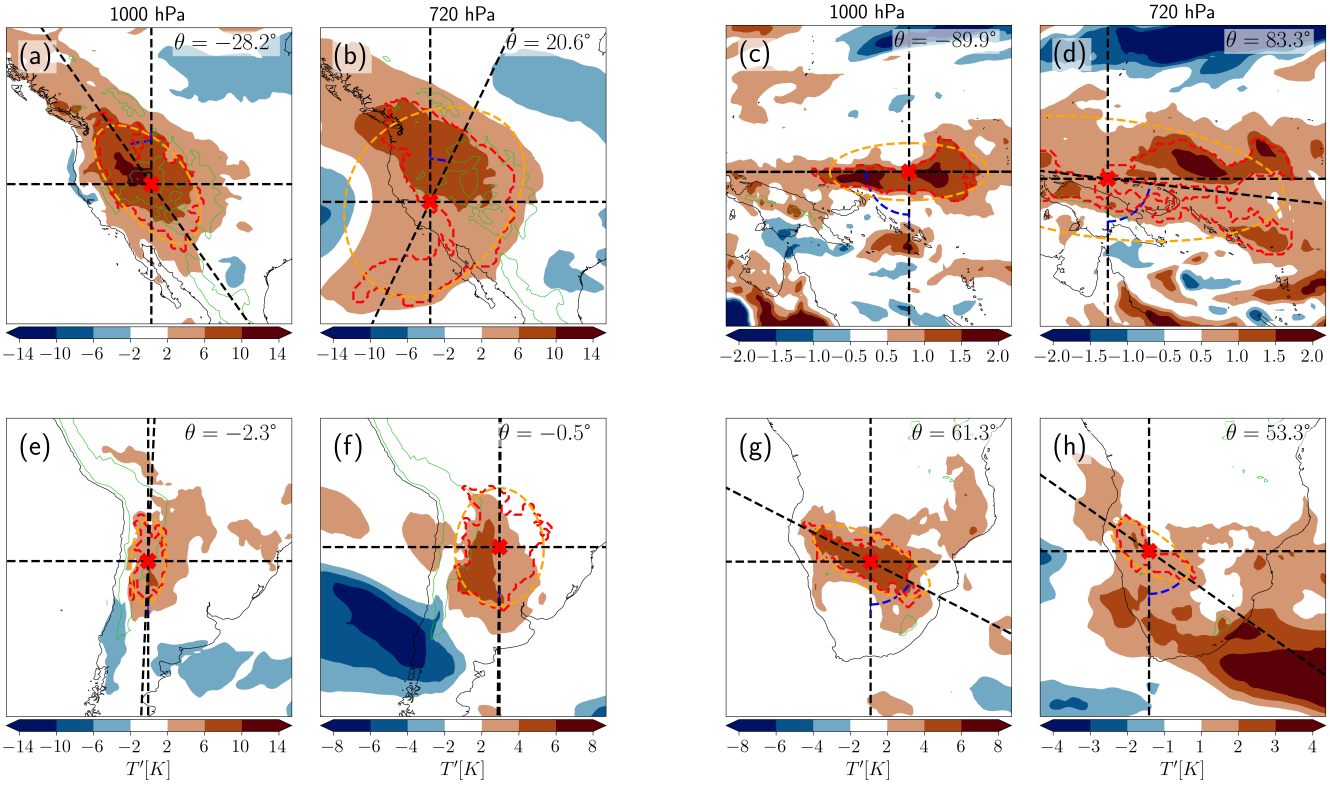


Figure 6. Examples of heat cell contours and their respective ellipse approximation at 1000 hPa and 720 hPa. Heat cells found in **(a, b)** the North American Rockies (40°N, 114°W) on 14 June 1974 ; **(c, d)** the equatorial Eastern Pacific (0°, 160°E) on 29 January 1952; **(e, f)** the South American Andes (27°S, 66°W) on 1 March 1966; and **(g, h)** South Africa (20°S, 23°E) on 23 December 1960. Colors show the temperature anomalies T', note that the color scales differ. As in Fig. 1, the red contours show the heat cells based on the 95th quantile and the orange contours show the ellipse approximation. Green contours indicate topographic features above 1750 m.

America and Europe at similar latitudes. North America is split in two at the surface, with its western part following mostly a meridional orientation along the Rockies and the eastern part having nearly zonal orientation of the ellipses. In contrast, Europe presents a more continuous distribution of the orientation angle, around 30 to 60°. These topographic influences are less visible at upper levels, as the orientation of heat cells is less influenced by surface processes and more by the free-troposphere dynamics (Fig. 5b,d). The weakening of topographic influences in the free atmosphere is also seen by comparing Fig. 6a to Fig. 6b, where the alignment with the Rockies for the surface heat cell changed to a more typical northeast-southwest orientation in the free troposphere mid-latitudes at 720 hPa. Finally, we note a reversal of the orientation angle towards negative values of around $-45°$for the high latitudes in both hemispheres, which may reflect different mechanisms leading to heat extremes in these regions compared to the anticyclonic structures in the mid-latitudes (Hotz et al., 2026). There is also some variability of the

https://doi.org/10.5194/egusphere-2026-5697
Preprint. Discussion started: 15 October 2026
© Author(s) 2026. CC BY 4.0 License.

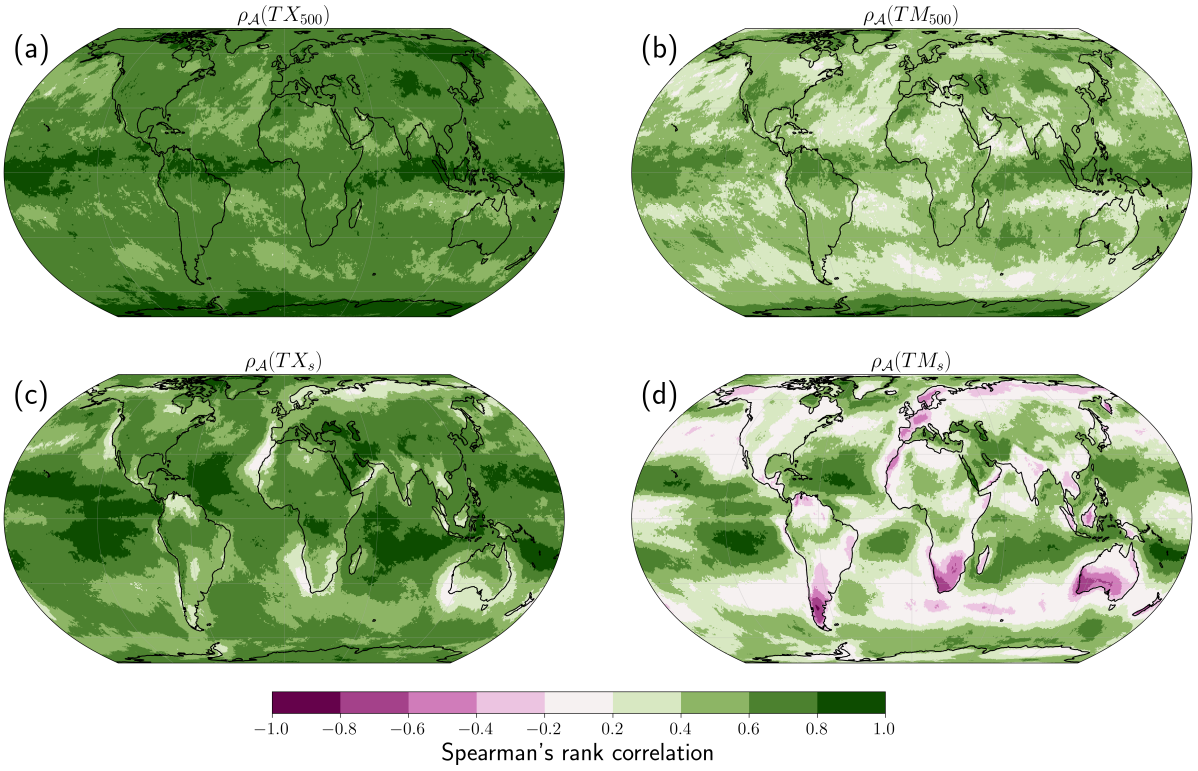


Figure 7. Spearman's rank correlation coefficient between heat cell area and intensity. Correlation between **(a)** maximum T' vs. area at 500 hPa, **(b)** mean T' vs. area at 500 hPa, **(c)** maximum T' vs. area at 1000 hPa, and (d) mean T' vs. area at 1000 hPa. Note that the number of events considered in the correlation is not the same at 1000 and 500 hPa.

orientation angle between individual heat cells in all regions and at the different vertical levels (Fig. A3), but this tends to be low and the average angle represents well the typical direction of heat cells.

3.3 Correlation of heat cell size and intensity

Finally, we explore the relationship between the intensity and the area of the identified heat cells. Overall, the area and intensity of heat cells are positively correlated globally for each intensity metric both at the surface and in the mid-troposphere (Fig. 7): larger heat cells tend to be more intense. An important exception is the correlation between the mean anomaly and the area at the surface (Fig. 7d): while there are usually positive correlations over subtropical highs for example, heat cells in western Europe show a slightly negative correlation between the mean surface intensity and the area, similar to the mid-latitudes land regions in the Southern Hemisphere. In North America, the correlation is weak, while it is stronger over China and the Middle East. However, when considering the maximum temperature anomaly (Fig. 7c), the correlations are much higher and systematic over the globe, typically above 0.8. In the mid-troposphere, the correlations are even more homogeneous and systematic for both the mean and maximum intensity, although with lower values for the former (Fig. 7a,b).

https://doi.org/10.5194/egusphere-2026-5697
Preprint. Discussion started: 15 October 2026
© Author(s) 2026. CC BY 4.0 License.

We hypothesize that the different behavior for $\rho_{\mathcal{A}}(TM_s)$ could be caused by turbulent mixing within the boundary layer. One supporting observation is that surfaces over subtropical highs, with a relatively stable boundary layer due to persistent air subsidence, have both highest $\rho_{\mathcal{A}}(TX_s)$ and $\rho_{\mathcal{A}}(TM_s)$, indicating that these regions also have the least deviations to the area-intensity relationship. This hypothesis could also explain the low $\rho_{\mathcal{A}}(TX_s)$ values and even negative $\rho_{\mathcal{A}}(TM_s)$ in many coastal areas, where sudden changes in surface roughness create the internal boundary layer, with more complex thermal and dynamical exchanges between the ground and the atmosphere (Krishnamurthy et al., 2023), potentially leading to the breakdown of the correlation. Meanwhile, the ocean regions with the lowest values of $\rho_{\mathcal{A}}(TM_s)$ seem to have no distinct pattern. Intuitively, a possible hypothesis could be that the $\rho_{\mathcal{A}}(TM_s)$ minima over the oceans are related to regions with strongly positive or negative ocean surface heat fluxes, since air–sea turbulent heat fluxes link strongly to changes in stability conditions in the marine atmospheric boundary layer (Song et al., 2024), which is likely to also modify the area-intensity relationship of near-surface heat cells. However, further analysis is required to validate the hypothesis.

4 Discussion

4.1 Evaluation of the heat cell detection and stacking algorithm

There are four main parameters in the heat cell stack identification algorithm introduced in Sect. 2.1 that our results may be sensitive to: the quantile chosen to identify the level of extremeness, the minimum $\mathcal{A}_{min}$ and maximum $\mathcal{A}_{max}$ areas for the heat cells detection, and the search radius R_{search} for attributing a heat cell at a certain level to a surface extreme. The choice of the 95th quantile to identify extremes is arbitrary, but it is a quantile that is often chosen in the literature on heatwaves (Barriopedro et al., 2023). Most quantitative results are sensitive to this choice, but insofar as we are using a local climatological quantile, we do not expect that the qualitative results such as the geographical differences would change massively. We tested the sensitivity of the detection and stacking algorithm by repeating the procedure with $\mathcal{A}_{min}$ set between $0\,\mathrm{km}^2$ to $3.141592 \times 10^7\,\mathrm{km}^2$, $\mathcal{A}_{max}$ set between $1.0 \times 10^7\,\mathrm{km}^2$ to $2.0 \times 10^7\,\mathrm{km}^2$, and R_{search} set between $500\,\mathrm{km}$ to $1000\,\mathrm{km}$. We qualitatively assessed and concluded that there are no major differences in the final results for this range of values of R_{search}. Meanwhile, a non-zero value of $\mathcal{A}_{min}$ is needed to filter out highly localized temperature anomaly spikes that are too small to be considered a heat cell. On the other hand, the value of $\mathcal{A}_{max}$ affects the average area extent of heat cells, particularly in the tropics, where we observed that outliers of large heat cell contours that are not characteristic of the typical structure of heat extremes appear in the upper troposphere if the value of $\mathcal{A}_{max}$ is above $2.5 \times 10^7\,\mathrm{km}^2$, or if the maximum contour area is not limited. A possible explanation is that positive T' anomalies at upper levels, linked to large scale modes of variability such as ENSO, for example, would overlap with the heat cell stack, and lead to the merging of the 95th percentile contour associated with two separate heat cells. This would violate a major assumption that each heat cell stack represents a unique heat extreme event. We found that setting the value of the maximum contour area $\mathcal{A}_{max}$ to $1.9 \times 10^7\,\mathrm{km}^2$ minimizes such misidentification, but this issue constitutes a limit of our procedure in the tropics.

Although complete elimination of such sources of error remains challenging, after averaging across all sampled heat cell contour stacks, we are able to obtain a smooth and continuous vertical heat cell area consistent with the findings of previous

https://doi.org/10.5194/egusphere-2026-5697
Preprint. Discussion started: 15 October 2026
© Author(s) 2026. CC BY 4.0 License.

studies, especially Hotz et al. (2026). It should be noted that the existence of merged contour instances is also the reason why, instead of directly checking for lateral overlaps of heat cell contours between neighboring vertical levels, we define a search area based on the *surface* heat cell contour for selecting contours belonging to the same heat extreme in the stacking algorithm. This is to avoid cases where an anomalously large merged contour is used for overlap checking and falsely identified contours very far away as part of the heat cell contour stack.

4.2 Heat cell geometry

We have shown that the axis ratio of the ellipses that best fit the heat cells geometry was remarkably constant in various regions of the globe, around 0.5–0.6. Accordingly, we could precisely define an orientation angle with respect to the pole in each hemisphere. In the mid-latitudes, this ellipse shape with a typical orientation angle around 60°is not surprising because it corresponds to the direction of anticyclonic wave breaking that is associated with the anticyclones promoting surface heat extremes (Weijenborg et al., 2012; Barriopedro et al., 2023). Another way to interpret this angle is the usually slightly positive phase speed of Rossby wave packets that occur in conjunction with stationary anticyclones (Röthlisberger et al., 2019; Jiménez-Esteve and Domeisen, 2022; Noyelle et al., 2025). However, the direction of Rossby wave breaking does not appear to explain the effect of large-scale topography on heat cell orientation, because surface heat cells near large mountains seem to be aligned with the orientation of the elevated terrain. As the effect seems to be very localized and not at the scale of the Rossby wave, an alternative mechanism could be that heat extremes with surface heat cells that are aligned with the topography are formed through foehn effects on the leeward slopes of mountains (Tan et al., 2024). The near-zonal orientation of the heat cells in the tropics is more mysterious and we are not aware of previous studies that systematically identified spatial mechanisms linked to temperature extremes in the tropics. Equatorial large-scale atmospheric waves are generally elongated in the zonal direction (Roundy and Frank, 2004; Knippertz et al., 2022), which may explain this result, but it is not clear whether and how they are related to surface heat extremes, especially over oceans where SST anomalies also tend to be zonally elongated (e.g. Vialard et al., 2025).

5 Conclusions

We have developed a novel, global heat cell contouring and stacking method to identify the 3D temperature anomaly structure in the troposphere associated with surface heat extremes. We have examined their geometric properties, including size, aspect ratio and orientations, and the geographical distribution of these properties globally. In addition, we have measured the link between the area and the intensity of heat cells at the surface and in the mid-troposphere. The main findings are as follows:

1. Globally, near-surface heat cells have a relatively uniform average area, corresponding to the area covered by a circle with an equivalent radius $r_{\mathcal{A}}$ of around 800 km. Surface heat cells in the tropics are on average larger than those at higher latitudes, especially over oceans. 3D temperature anomalies in the tropics have a significantly lower vertical extent than those in the extratropics, with the former being mostly confined to the lower troposphere.

https://doi.org/10.5194/egusphere-2026-5697
Preprint. Discussion started: 15 October 2026
© Author(s) 2026. CC BY 4.0 License.

2. The shape of heat cells at the surface and in the middle to upper troposphere is not circular. Heat cells are mostly elliptical, with a ratio of 0.5–0.6 between the semi-minor and semi-major axes lengths, which is remarkably uniform across the globe.

3. Heat cells have a systematic preferential orientation that is mostly dependent on latitude and local topography. While tropical heat cells are mostly zonally oriented, the orientation of heat cells leans poleward towards higher latitudes, following the direction of anticyclonic wave breaking in each hemisphere. High-elevation mountain ranges massively influence the orientation of heat cells near the surface.

4. There is a robust positive correlation between the intensity and the area of heat cells in the mid-troposphere: more extreme events tend to be larger. While the relationship is also present at the surface for the maximum intensity, it is weaker for the mean intensity of heat cells.

Our results provide a global and systematic description of the 3D temperature anomalies associated with surface heat extremes. In recent years, the vertical shape of temperature anomalies during heatwaves — especially in mid-latitudes — has been described as a so-called “heat dome” (Zhang et al., 2023; Jain et al., 2024; Li et al., 2024). Based on our results, we think this simplified image can be misleading. Although it is true that during surface heat extremes the temperature anomalies extend throughout the troposphere in the mid-latitudes, as already shown systematically by Hotz et al. (2026), the horizontal shapes of those anomalies are clearly not circular as implied by the image of a dome. In addition, in the tropics, the image of a “heat dome” is misleading because the temperature anomalies do not extend throughout the troposphere. Finally, the image of the “heat dome” gives an implicit idea that the mechanisms leading to temperature anomalies throughout the troposphere are horizontally and vertically uniform, despite scientific evidence that they are not (Zschenderlein et al., 2020; Neal et al., 2022; Schumacher et al., 2022; Hotz et al., 2024). We thus advocate against the use of this image and terminology for describing the 3D temperature anomaly structure associated to surface heat extremes in the scientific literature.

https://doi.org/10.5194/egusphere-2026-5697
Preprint. Discussion started: 15 October 2026
© Author(s) 2026. CC BY 4.0 License.

Appendix A: Additional figures

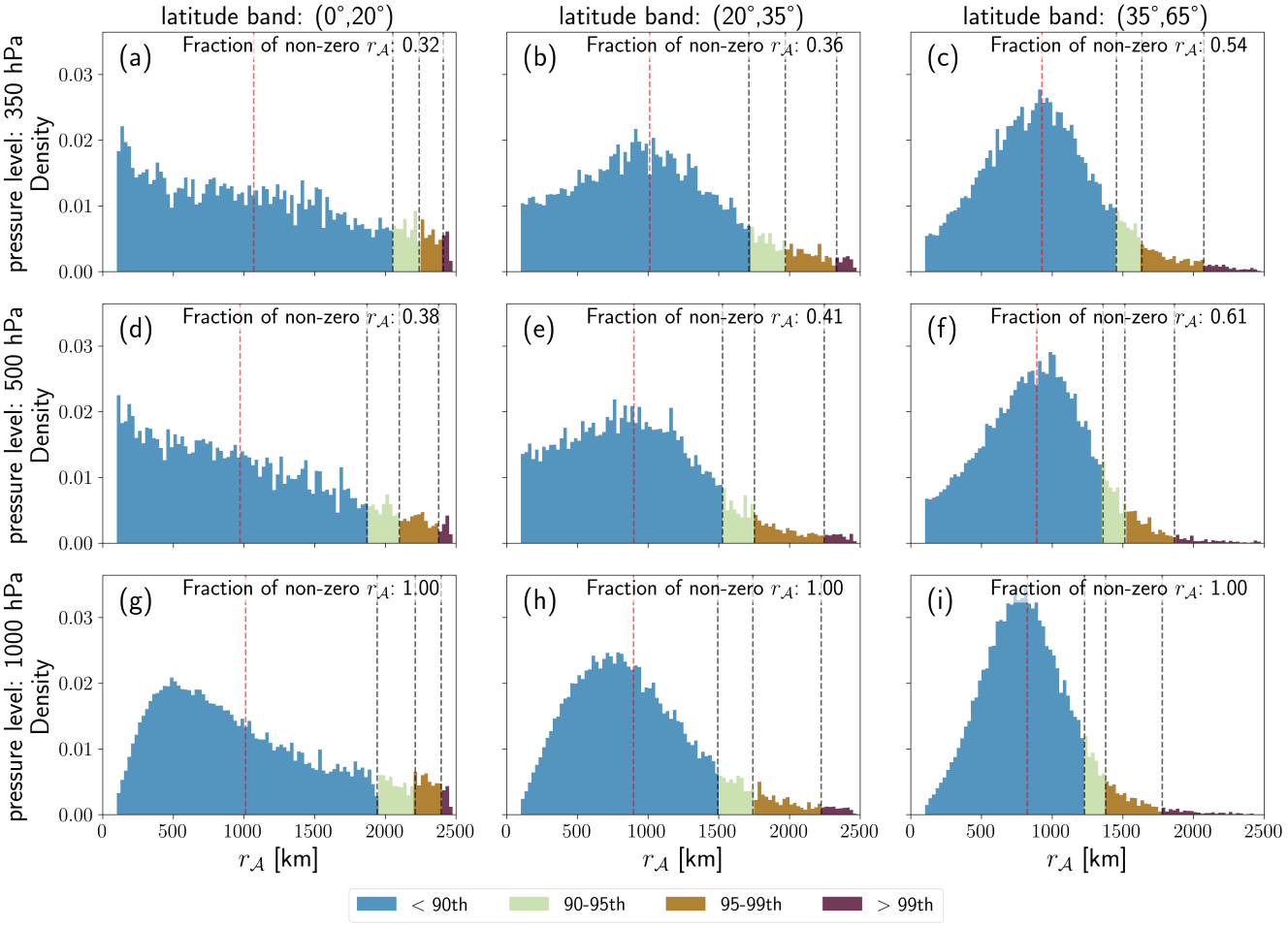


Figure A1. Distribution of equivalent radius $r_{\mathcal{A}}$ values for every heat cells in three latitude bands. **(a, d, g)** Deep tropics (20°S–20°N), (b,e,h) sub-tropics (20°S–35°S and 20°N–35°N), and **(c, f, i)** mid-latitudes (35°S–65°S and 35°N–65°N). The distributions are shown at three vertical pressure levels with reference to a surface pressure level of 1000 hPa: (a,b,c) 350 hPa, **(d, e, f)** 500 hPa, and (g,h,i) 1000 hPa. Bars with different colors separated by vertical, gray dotted lines corresponds to data below the 90th percentile (blue), between 90th–95th percentiles (green), between 95th–99th percentiles (brown) and above the 99th percentile (purple). Red dotted lines show the mean of each distributions. The fraction of non-zero $r_{\mathcal{A}}$ refers to the ratio of data points where a heat cell is presented with a non-zero area extent to the total number of heat cell stack samples in each distribution.

https://doi.org/10.5194/egusphere-2026-5697
Preprint. Discussion started: 15 October 2026
© Author(s) 2026. CC BY 4.0 License.

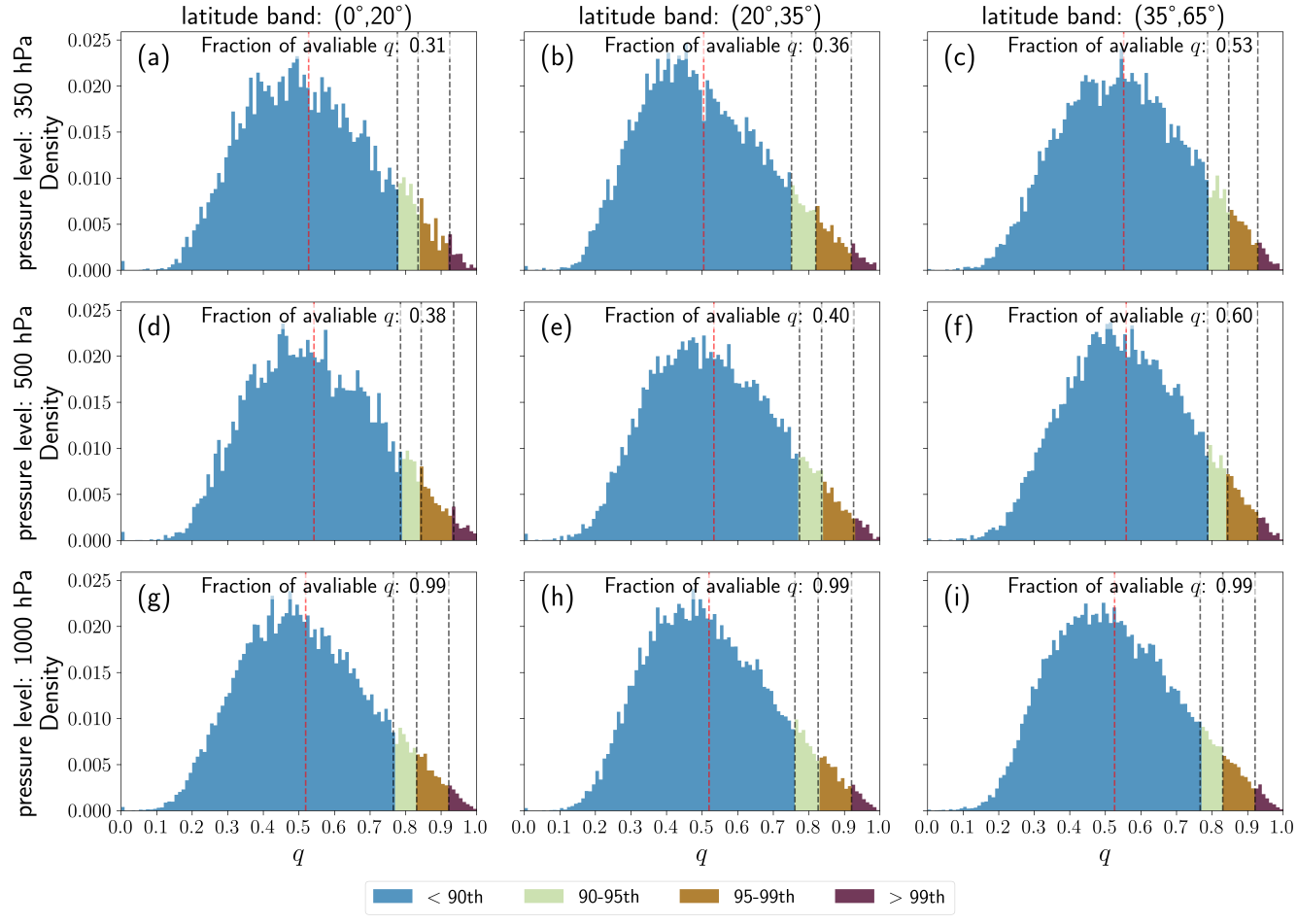


Figure A2. As Fig. A1 for axes ratio q.

https://doi.org/10.5194/egusphere-2026-5697
Preprint. Discussion started: 15 October 2026
© Author(s) 2026. CC BY 4.0 License.

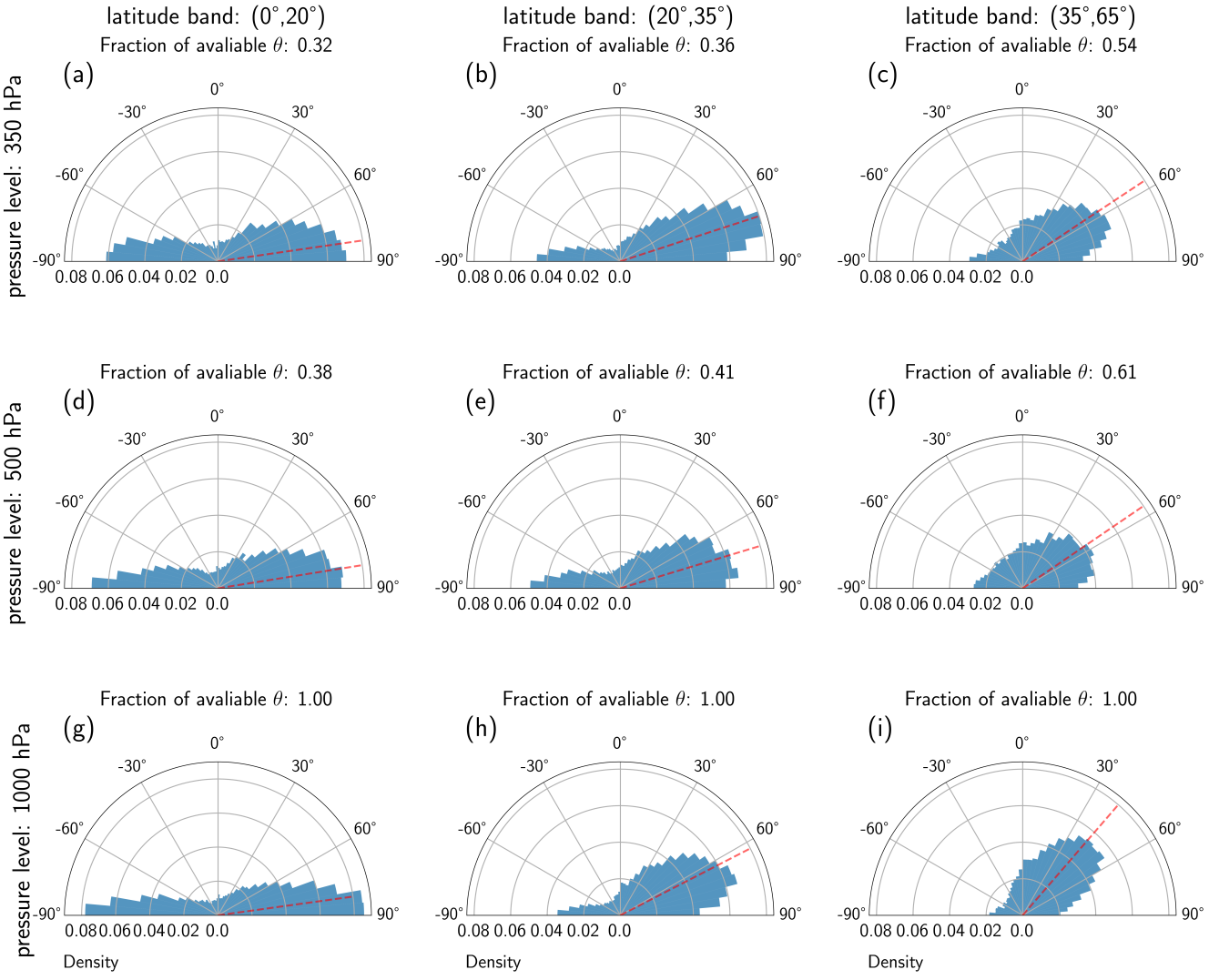


Figure A3. As Fig. A1 for ellipse orientation angles θ. Red dotted lines are the circular mean of each distributions. Note that the angle value is with respect to the hemispheric poles of individual grid points.

https://doi.org/10.5194/egusphere-2026-5697
Preprint. Discussion started: 15 October 2026
© Author(s) 2026. CC BY 4.0 License.

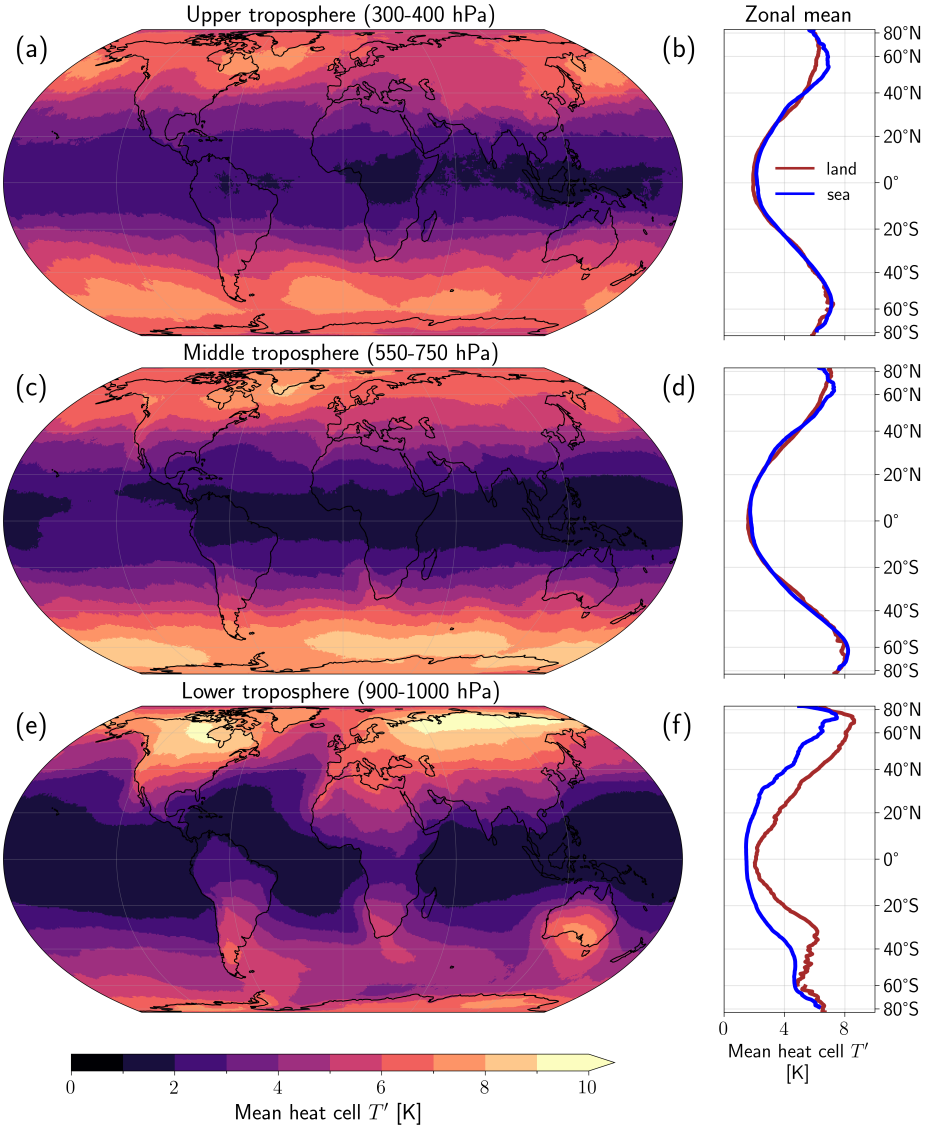


Figure A4. As Fig. 4 for the mean values of T' in heat cells.

https://doi.org/10.5194/egusphere-2026-5697
Preprint. Discussion started: 15 October 2026
© Author(s) 2026. CC BY 4.0 License.

Appendix B: Heat cell vertices re-projection for ellipse approximation

To simplify the process of least-square ellipse approximation of heat cells, the calculation of the best-fit ellipse (shown in appendix C) is done on a local Cartesian plane instead of directly over Earth's surface. For each set of longitude-latitude coordinate pairs $\{(\lambda_i, \varphi_i)\}_{i=1}^{n}$ that represents a heat cell contour on the Earth's surface, we choose the centroid $\mathbf{c} := (\lambda_c, \varphi_c)$ to be the tangent point of the local Cartesian plane relative to the Earth's surface. Then, each pair of longitude-latitude coordinates (λ, φ) is mapped to the planar coordinate (x_i, y_i) such that the distance and bearing of the original heat cell contour are preserved (Hofmann-wellenhof and Moritz, 2006). The angular distance c_i between a vertex (λ_i, φ_i) and the centroid (λ_c, φ_c) is:

$$c_i = \arccos\left[\sin\phi_0 \sin\phi + \cos\phi_0 \cos\phi \cos(\lambda - \lambda_0)\right]. \tag{B1}$$

The forward azimuth γ between a vertex (λ_i, φ_i) and the centroid (λ_c, φ_c) is:

$$\gamma_i = \operatorname{atan2}\left[\cos\phi_i \sin(\lambda_i - \lambda_0),\ \cos\phi_0 \sin\phi_i - \sin\phi_0 \cos\phi_i \cos(\lambda_i - \lambda_0)\right]. \tag{B2}$$

Assuming spherical Earth, the corresponding planar coordinate vertex, scaled by Earth Radius R will therefore be:

$$x_i = Rc_i \sin\gamma_i \qquad y_i = Rc_i \cos\gamma_i. \tag{B3}$$

The assumption that the ellipse fitted to the contour exists on a planar surface rather than the Earth's surface leads to deviations in the measurement of the semi-major and semi-minor axes lengths, in which the size of the error depends on whether the size of the ellipse is comparable to the Earth's curvature. Let us assume a heat cell length scale of around $1000\,\mathrm{km}$. The difference between a straight-line distance c and the arc-length s on the Earth's surface is:

$$\Delta = s - c = R\theta - 2R\sin\left(\frac{\theta}{2}\right), \tag{B4}$$

where θ is the latitude range. Given the arc-length $s = 1000\,\mathrm{km}$, the corresponding straight-line distance will therefore be:

$$\theta = \frac{s}{R} = \frac{1000}{6370} \approx 0.16\,\mathrm{rad}, \tag{B5}$$

which leads to:

$$c = 2(6370)\sin\left(\frac{0.16}{2}\right) \simeq 998.97\,\mathrm{km}. \tag{B6}$$

This implies an error $\Delta \simeq 1.03\,\mathrm{km}$, or around 0.1%.

Meanwhile, the RMSE of the least-square ellipse fit would be:

$$\mathrm{RMSE} = \sqrt{\frac{1}{N}\sum_{i=1}^{N} d_i^2} \approx 100\,\mathrm{km}, \tag{B7}$$

where d_i is the (Euclidean) distance from the data point i to the fitted ellipse (in meters), and N is the total number of data points.

https://doi.org/10.5194/egusphere-2026-5697
Preprint. Discussion started: 15 October 2026
© Author(s) 2026. CC BY 4.0 License.

Appendix C: Derivation of ellipse parameters

The lengths of the semi-major and semi-minor axes (a, b) and the orientation angle of the ellipse (θ) are the geometric parameters summarizing the shape of the ellipse approximating the heat cell contour. They can be derived following the methods in classical conic geometric analytics (Chávez-Pichardo et al., 2025).

The quadratic coefficient matrix of the conic equation Q can be written as:

$$Q = \begin{pmatrix} \hat{A} & \frac{\hat{B}}{2} \\ \frac{\hat{B}}{2} & \hat{C} \end{pmatrix}. \tag{C1}$$

The constant term F_0, the eigenvalues λ_1, λ_2 of Q are then:

$$F_0 := \hat{F} - \frac{\hat{C}\hat{D}^2 - \hat{B}\hat{D}\hat{E} + \hat{A}\hat{E}^2}{4(B^2 - 4AC)}, \tag{C2}$$

$$\lambda_{1,2} := \frac{\hat{A} + \hat{C} \pm \sqrt{(\hat{A} - \hat{C})^2 + \hat{B}^2}}{2}, (\lambda_1 \leq \lambda_2), \tag{C3}$$

where $(\hat{A}, \hat{B}, \hat{C}, \hat{D}, \hat{E}, \hat{F})$ are the estimated conic coefficients as described in Sect. 2.3.

The semi-major axis a and semi-minor axis b are therefore:

$$a = \sqrt{\frac{-F_0}{\lambda_1}}, \qquad b = \sqrt{\frac{-F_0}{\lambda_2}}, \qquad (a \geq b). \tag{C4}$$

Meanwhile, the rotation angle θ of the ellipse (from the y-axis to the ellipse's principal axes in the local Cartesian plane) can be expressed in a simplified expression as:

$$\theta = \frac{1}{2} \arctan2\big(\hat{B},\ \hat{A} - \hat{C}\big), \tag{C5}$$

which is obtained by first rotating the coordinate system to align with the orientation of the ellipse (Chávez-Pichardo et al., 2025).

Author contributions. All authors contributed to the conceptualization of the study and the editing of the text. HL, RN and BH developed the method and wrote the first draft; HL investigated and visualized the data.

Competing interests. One of the authors (H. Wernli) is editor of *Weather and Climate Dynamics*.

https://doi.org/10.5194/egusphere-2026-5697
Preprint. Discussion started: 15 October 2026
© Author(s) 2026. CC BY 4.0 License.



Acknowledgements. AI-powered search engines were used strictly for parts of code development and formatting of mathematical equations (OpenAI ChatGPT and Anthropic Claude). We also acknowledge Crameri et al. (2020) for the scientific color maps, which were used in most of the figures. RN has received funding from the Swiss National Science Foundation (SNSF) via grant no. 216710.

https://doi.org/10.5194/egusphere-2026-5697
Preprint. Discussion started: 15 October 2026
© Author(s) 2026. CC BY 4.0 License.

References

Barriopedro, D., García-Herrera, R., Ordóñez, C., Miralles, D. G., and Salcedo-Sanz, S.: Heat waves: physical understanding and scientific challenges, Rev. Geophys., 61, e2022RG000780, https://doi.org/10.1029/2022RG000780, _eprint: https://agupubs.onlinelibrary.wiley.com/doi/pdf/10.1029/2022RG000780, 2023.

Blanchard-Wrigglesworth, E., Cox, T., Espinosa, Z. I., and Donohoe, A.: The largest ever recorded heatwave—characteristics and attribution of the Antarctic heatwave of March 2022, Geophys. Res. Lett., 50, e2023GL104910, https://doi.org/10.1029/2023GL104910, 2023.

Brunner, L. and Steiner, A. K.: A global perspective on atmospheric blocking using GPS radio occultation – one decade of observations, Atmos. Meas. Tech., 10, 4727–4745, https://doi.org/10.5194/amt-10-4727-2017, 2017.

Brunner, L., Steiner, A. K., Scherllin-Pirscher, B., and Jury, M. W.: Exploring atmospheric blocking with GPS radio occultation observations, Atmos. Chem. Phys., 16, 4593–4604, https://doi.org/10.5194/acp-16-4593-2016, 2016.

Byrne, M. P.: Amplified warming of extreme temperatures over tropical land, Nat. Geosci., 14, 837–841, https://doi.org/10.1038/s41561-021-00828-8, 2021.

Cebrián, A. C., Asín, J., Gelfand, A. E., Schliep, E. M., Castillo-Mateo, J., Beamonte, M. A., and Abaurrea, J.: Spatio-temporal analysis of the extent of an extreme heat event, Stoch. Environ. Res. Risk Assess., 36, 2737–2751, https://doi.org/10.1007/s00477-021-02157-z, 2022.

Chávez-Pichardo, M., López-Barrientos, J. D., and Perea-Flores, S.: A unified general theory of conic sections via the conic radical, Mathematics, 14, 138, https://doi.org/10.3390/math14010138, 2025.

Costa, D. F., Gomes, H. B., Silva, M. C. L., and Zhou, L.: The most extreme heat waves in Amazonia happened under extreme dryness, Clim. Dyn., 59, 281–295, https://doi.org/10.1007/s00382-021-06134-8, 2022.

Crameri, F., Shephard, G. E., and Heron, P. J.: The misuse of colour in science communication, Nat. Commun., 11, 5444, https://doi.org/10.1038/s41467-020-19160-7, 2020.

Domeisen, D. I. V., Eltahir, E. A. B., Fischer, E. M., Knutti, R., Perkins-Kirkpatrick, S. E., Schär, C., Seneviratne, S. I., Weisheimer, A., and Wernli, H.: Prediction and projection of heatwaves, Nat. Rev. Earth Environ., 4, 36–50, https://doi.org/10.1038/s43017-022-00371-z, 2023.

Duan, S. Q., Ahmed, F., and Neelin, J. D.: Moist heatwaves intensified by entrainment of dry air that limits deep convection, Nat. Geosci., 17, 837–844, https://doi.org/10.1038/s41561-024-01498-y, 2024.

Elvidge, A. D. and Renfrew, I. A.: The causes of foehn warming in the lee of mountains, Bull. Am. Meteorol. Soc., 97, 455–466, https://doi.org/10.1175/BAMS-D-14-00194.1, 2016.

Evenden, G. I., Rouault, E., Warmerdam, F., Evers, K., Knudsen, T., Butler, H., Taves, M. W., Schwehr, K., Sales de Andrade, E., Karney, C., Couwenberg, S., Dawson, N., Snow, A. D., and Jimenez Shaw, J.: PROJ, https://doi.org/10.5281/ZENODO.5884394, 2026.

Happé, T., Wijnands, J. S., Fernández-Torres, M. A., Scussolini, P., Muntjewerf, L., and Coumou, D.: Detecting sSpatiotemporal dynamics of western European heatwaves using deep learning, Artif. Intell. Earth Syst., 3, https://doi.org/10.1175/AIES-D-23-0107.1, 2024.

Hofmann-wellenhof, B. and Moritz, H.: Physical Geodesy, Springer Vienna, 2 edn., ISBN 978-3-211-33544-4, https://doi.org/10.1007/978-3-211-33545-1, 2006.

Hotz, B., Papritz, L., and Röthlisberger, M.: Understanding the vertical temperature structure of recent record-shattering heatwaves, Weather Clim. Dynam., 5, 323–343, https://doi.org/10.5194/wcd-5-323-2024, 2024.

https://doi.org/10.5194/egusphere-2026-5697
Preprint. Discussion started: 15 October 2026
© Author(s) 2026. CC BY 4.0 License.

Hotz, B., Wernli, H., Röthlisberger, M., and Noyelle, R.: Global characterisation of the vertical temperature anomaly structure of heat extremes over land in ERA5, https://doi.org/10.5194/egusphere-2026-1522, 2026.

Jain, P., Sharma, A. R., Acuna, D. C., Abatzoglou, J. T., and Flannigan, M.: Record-breaking fire weather in North America in 2021 was initiated by the Pacific northwest heat dome, Commun. Earth Environ., 5, 202, https://doi.org/10.1038/s43247-024-01346-2, 2024.

Jiménez-Esteve, B. and Domeisen, D. I.: The role of atmospheric dynamics and large-scale topography in driving heatwaves, Q. J. R. Meteorol. Soc., 148, 2344–2367, https://doi.org/10.1002/qj.4306, 2022.

Jiménez-Esteve, B., Kornhuber, K., and Domeisen, D. I. V.: Heat extremes driven by amplification of phase-locked circumglobal waves forced by topography in an idealized atmospheric model, Geophys. Res. Lett., 49, e2021GL096 337, https://doi.org/10.1029/2021GL096337, 2022.

Jin, Z., Xu, K., Ge, F., Wang, W., and Lin, Z.: Boost to early spring compound heatwaves over South Asia from anomalous Tibetan Plateau atmospheric heat source, Atmos. Res., 305, 107 449, https://doi.org/10.1016/j.atmosres.2024.107449, 2024.

Joshi, M. M., Gregory, J. M., Webb, M. J., Sexton, D. M. H., and Johns, T. C.: Mechanisms for the land/sea warming contrast exhibited by simulations of climate change, Clim. Dyn., 30, 455–465, https://doi.org/10.1007/s00382-007-0306-1, 2008.

Knippertz, P., Gehne, M., Kiladis, G. N., Kikuchi, K., Rasheeda Satheesh, A., Roundy, P. E., Yang, G.-Y., Žagar, N., Dias, J., Fink, A. H., Methven, J., Schlueter, A., Sielmann, F., and Wheeler, M. C.: The intricacies of identifying equatorial waves, Q. J. R. Meteorol. Soc., 148, 2814–2852, https://doi.org/10.1002/qj.4338, 2022.

Kornhuber, K., Petoukhov, V., Petri, S., Rahmstorf, S., and Coumou, D.: Evidence for wave resonance as a key mechanism for generating high-amplitude quasi-stationary waves in boreal summer, Clim. Dyn., 49, 1961–1979, https://doi.org/10.1007/s00382-016-3399-6, 2017.

Krishnamurthy, R., Fernando, H. J. S., Alappattu, D., Creegan, E., and Wang, Q.: Observations of offshore internal boundary layers, J. Geophys. Res. D: Atmos., 128, e2022JD037 425, https://doi.org/10.1029/2022JD037425, 2023.

Kumar, M.: World geodetic system 1984: A modern and accurate global reference frame, Mar. Geod., 12, 117–126, https://doi.org/10.1080/15210608809379580, 1988.

Lembo, V., Bordoni, S., Bevacqua, E., Domeisen, D. I. V., Franzke, C. L. E., Galfi, V. M., Garfinkel, C. I., Grams, C. M., Hochman, A., Jha, R., Kornhuber, K., Kwasniok, F., Lucarini, V., Messori, G., Pappert, D., Perez-Fernandez, I., Riboldi, J., Russo, E., Shaw, T. A., Strigunova, I., Strnad, F., Yiou, P., and Zagar, N.: Dynamics, statistics, and predictability of Rossby waves, heat waves, and spatially compounding extreme events, Bull. Am. Meteorol. Soc., 105, E2283–E2293, https://doi.org/10.1175/BAMS-D-24-0145.1, 2024.

Lhotka, O. and Kyselý, J.: Three-dimensional analysis reveals diverse heat wave types in Europe, Commun. Earth Environ., 5, 323, https://doi.org/10.1038/s43247-024-01497-2, 2024.

Li, F. and Tamarin-Brodsky, T.: Atmospheric stability sets maximum moist heat and convection in the midlatitudes, Sci. Adv., 12, eaea8453, https://doi.org/10.1126/sciadv.aea8453, 2026.

Li, X., Mann, M. E., Wehner, M. F., Rahmstorf, S., Petri, S., Christiansen, S., and Carrillo, J.: Role of atmospheric resonance and land–atmosphere feedbacks as a precursor to the June 2021 Pacific Northwest Heat Dome event, Proc. Natl. Acad. Sci. U.S.A., 121, e2315330 121, https://doi.org/10.1073/pnas.2315330121, 2024.

Lopes, F. M., Dutra, E., and Boussetta, S.: Evaluation of daily temperature extremes in the ECMWF operational weather forecasts and ERA5 reanalysis, Atmosphere, 15, 93, https://doi.org/10.3390/atmos15010093, 2024.

Luo, M., Lau, N.-C., Liu, Z., Wu, S., and Wang, X.: An observational investigation of spatiotemporally contiguous heatwaves in China from a 3D perspective, Geophys. Res. Lett., 49, e2022GL097 714, https://doi.org/10.1029/2022GL097714, 2022.

https://doi.org/10.5194/egusphere-2026-5697
Preprint. Discussion started: 15 October 2026
© Author(s) 2026. CC BY 4.0 License.

Lyon, B., Barnston, A. G., Coffel, E., and Horton, R. M.: Projected increase in the spatial extent of contiguous US summer heat waves and associated attributes, Environ. Res. Lett., 14, 114 029, https://doi.org/10.1088/1748-9326/ab4b41, 2019.

Maple, C.: Geometric design and space planning using the marching squares and marching cube algorithms, in: 2003 International Conference on Geometric Modeling and Graphics, 2003. Proceedings, pp. 90–95, IEEE Comput. Soc, London, UK, ISBN 978-0-7695-1985-2, https://doi.org/10.1109/GMAG.2003.1219671, 2003.

Mardia, K. V. and Jupp, P. E.: Directional Statistics, Wiley Series in Probability and Statistics, Wiley, 1 edn., ISBN 978-0-471-95333-3 978-0-470-31697-9, https://doi.org/10.1002/9780470316979, 1999.

Mayer, A.: A new global Lagrangian analysis of near-surface temperature extremes, Geophys. Res. Lett., 52, e2025GL116 696, https://doi.org/10.1029/2025GL116696, 2025.

McGregor, G.: Synoptic scale atmospheric processes and heatwaves, in: Heatwaves, vol. 6, pp. 207–259, Springer International Publishing, Cham, ISBN 978-3-031-69905-4 978-3-031-69906-1, https://doi.org/10.1007/978-3-031-69906-1_6, series Title: Biometeorology, 2024.

Miralles, D. G., Teuling, A. J., van Heerwaarden, C. C., and Vilà-Guerau de Arellano, J.: Mega-heatwave temperatures due to combined soil desiccation and atmospheric heat accumulation, Nat. Geosci., 7, 345–349, https://doi.org/10.1038/ngeo2141, 2014.

Miralles, D. G., Gentine, P., Seneviratne, S. I., and Teuling, A. J.: Land–atmospheric feedbacks during droughts and heatwaves: state of the science and current challenges, Ann. N. Y. Acad. Sci., 1436, 19–35, https://doi.org/10.1111/nyas.13912, _eprint: https://nyaspubs.onlinelibrary.wiley.com/doi/pdf/10.1111/nyas.13912, 2019.

Nabizadeh, E., Lubis, S. W., and Hassanzadeh, P.: The 3D structure of northern hemisphere blocking events: climatology, role of moisture, and response to climate change, J. Clim., 34, 9837–9860, https://doi.org/10.1175/JCLI-D-21-0141.1, 2021.

Neal, E., Huang, C. S. Y., and Nakamura, N.: The 2021 Pacific northwest heat wave and associated blocking: meteorology and the role of an upstream cyclone as a diabatic source of wave activity, Geophys. Res. Lett., 49, e2021GL097 699, https://doi.org/10.1029/2021GL097699, 2022.

Nicolas, Q. and Hotz, B.: Dry and moist convective upper bounds for near-surface temperatures, Weather Clim. Dynam., 7, 843–856, https://doi.org/10.5194/wcd-7-843-2026, 2026.

Noyelle, R., Caubel, A., Meurdesoif, Y., Faranda, D., and Yiou, P.: Evolution of the dDynamics of centennial hot summers in western Europe with climate change, Geophys. Res. Lett., 52, e2025GL115 552, https://doi.org/10.1029/2025GL115552, 2025.

Noyelle, R., Robin, Y., Naveau, P., Yiou, P., and Faranda, D.: Integration of physical bound constraints to alleviate shortcomings of statistical models for extreme temperatures, J. Clim., 39, 1457–1484, https://doi.org/10.1175/JCLI-D-25-0112.1, 2026.

Oertel, A., Pickl, M., Quinting, J. F., Hauser, S., Wandel, J., Magnusson, L., Balmaseda, M., Vitart, F., and Grams, C. M.: Everything hits at once: How remote rainfall matters for the prediction of the 2021 north American heat wave, Geophys. Res. Lett., 50, e2022GL100 958, https://doi.org/10.1029/2022GL100958, 2023.

O'Gorman, P. A. and Schneider, T.: The physical basis for increases in precipitation extremes in simulations of 21st-century climate change, Proc. Natl. Acad. Sci. U.S.A., 106, 14 773–14 777, https://doi.org/10.1073/pnas.0907610106, 2009.

Papritz, L.: Arctic lower-tropospheric warm and cold extremes: Horizontal and vertical transport, diabatic processes, and linkage to synoptic circulation Features, J. Clim., 33, 993–1016, https://doi.org/10.1175/JCLI-D-19-0638.1, 2020.

Plavcová, E., Lhotka, O., and Kyselý, J.: Heat waves in regional climate models: Three-dimensional insight and links to atmospheric circulation over middle Europe, Geophys. Res. Lett., 52, e2025GL115 352, https://doi.org/10.1029/2025GL115352, 2025.

Poppová, Z., Lhotka, O., Stryhal, J., and Kyselý, J.: Climatological characteristics and atmospheric circulation associated with three-dimensional heat wave types in middle Europe, Earth Space Sci., 13, e2025EA004 784, https://doi.org/10.1029/2025EA004784, 2026.

https://doi.org/10.5194/egusphere-2026-5697
Preprint. Discussion started: 15 October 2026
© Author(s) 2026. CC BY 4.0 License.



Roundy, P. E. and Frank, W. M.: A climatology of waves in the equatorial region, J. Atmos. Sci., 61, 2105–2132, https://doi.org/10.1175/1520-0469(2004)061<2105:ACOWIT>2.0.CO;2, 2004.

Röthlisberger, M. and Papritz, L.: Quantifying the physical processes leading to atmospheric hot extremes at a global scale, Nat. Geosci., 16, 210–216, https://doi.org/10.1038/s41561-023-01126-1, 2023.

Röthlisberger, M., Frossard, L., Bosart, L. F., Keyser, D., and Martius, O.: Recurrent synoptic-scale Rossby wave patterns and their effect on the persistence of cold and hot spells, J. Clim., 32, 3207–3226, https://doi.org/10.1175/JCLI-D-18-0664.1, 2019.

Schumacher, D. L., Hauser, M., and Seneviratne, S. I.: Drivers and mechanisms of the 2021 Pacific northwest heatwave, Earth's Future, 10, e2022EF002 967, https://doi.org/10.1029/2022EF002967, 2022.

Seneviratne, S. I., Corti, T., Davin, E. L., Hirschi, M., Jaeger, E. B., Lehner, I., Orlowsky, B., and Teuling, A. J.: Investigating soil moisture–climate interactions in a changing climate: A review, Earth-Sci. Rev., 99, 125–161, https://doi.org/10.1016/j.earscirev.2010.02.004, 2010.

Seneviratne, S. I., Zhang, X., Adnan, M., Badi, W., Dereczynski, C., Di Luca, A., Ghosh, S., Iskandar, I., Kossin, J., Lewis, S., Otto, F., Pinto, I., Satoh, M., Vicente-Serrano, S. M., Wehner, M., and Zhou, B.: Weather and climate extreme events in a changing Climate, in: Climate Change 2021: The physical science basis. Contribution of working Group I to the sixth assessment report of the Intergovernmental Panel on Climate Change, edited by Masson-Delmotte, V., Zhai, P., Pirani, A., Connors, S. L., Péan, C., Berger, S., Caud, N., Chen, Y., Goldfarb, L., Gomis, M. I., Huang, M., Leitzell, K., Lonnoy, E., Matthews, J. B. R., Maycock, T. K., Waterfield, T., Yelekçi, O., Yu, R., and Zhou, B., pp. 1513–1766, Cambridge University Press, Cambridge, UK and New York, NY, USA, https://doi.org/10.1017/9781009157896.013, 2021.

Soci, C., Hersbach, H., Simmons, A., Poli, P., Bell, B., Berrisford, P., Horányi, A., Muñoz-Sabater, J., Nicolas, J., Radu, R., Schepers, D., Villaume, S., Haimberger, L., Woollen, J., Buontempo, C., and Thépaut, J.: The ERA5 global reanalysis from 1940 to 2022, Quart. J. Royal Meteoro. Soc., 150, 4014–4048, https://doi.org/10.1002/qj.4803, 2024.

Song, X., Xie, X., Yan, Y., and Xie, S.-P.: Observed subdaily variations in air–sea turbulent heat fluxes under different marine atmospheric boundary layer stability conditions in the Gulf stream, Mon. Weather Rev., 152, 1223–1238, https://doi.org/10.1175/MWR-D-24-0003.1, 2024.

Tan, Z., Liu, Y., Li, D., Tang, W., Gao, J., and Dong, X.: Impacts of massive topographies on heat waves in global drylands, Geophys. Res. Lett., 51, e2024GL109 979, https://doi.org/10.1029/2024GL109979, 2024.

Vakrat, E. and Kushner, P. J.: Dynamical systems methods to understand projected heatwave intensification, Weather Clim. Extrem., 49, 100 791, https://doi.org/10.1016/j.wace.2025.100791, 2025.

Vialard, J., Jin, F.-F., McPhaden, M. J., Fedorov, A., Cai, W., An, S.-I., Dommenget, D., Fang, X., Stuecker, M. F., Wang, C., Wittenberg, A., Zhao, S., Liu, F., Kim, S.-K., Planton, Y., Geng, T., Lengaigne, M., Capotondi, A., Chen, N., Geng, L., Hu, S., Izumo, T., Kug, J.-S., Luo, J.-J., McGregor, S., Pagli, B., Priya, P., Stevenson, S., and Thual, S.: The El Niño Southern Oscillation (ENSO) recharge oscillator conceptual model: Achievements and future prospects, Rev. Geophys., 63, e2024RG000 843, https://doi.org/10.1029/2024RG000843, 2025.

Wang, H., Gao, Y., Wang, Y., and Sheng, L.: Arctic sea ice modulation of summertime heatwaves over western North America in recent decades, Environ. Res. Lett., 17, 074 015, https://doi.org/10.1088/1748-9326/ac765a, 2022.

Wehrli, K., Guillod, B. P., Hauser, M., Leclair, M., and Seneviratne, S. I.: Identifying key driving processes of major recent heat waves, J. Geophys. Res. D: Atmos., 124, 11 746–11 765, https://doi.org/10.1029/2019JD030635, 2019.

https://doi.org/10.5194/egusphere-2026-5697
Preprint. Discussion started: 15 October 2026
© Author(s) 2026. CC BY 4.0 License.

Weijenborg, C., de Vries, H., and Haarsma, R. J.: On the direction of Rossby wave breaking in blocking, Clim. Dyn., 39, 2823–2831, https://doi.org/10.1007/s00382-012-1332-1, 2012.

Wicker, W., Harnik, N., Pyrina, M., and Domeisen, D. I. V.: Heatwave location changes in relation to Rossby wave phase speed, Geophys. Res. Lett., 51, e2024GL108 159, https://doi.org/10.1029/2024GL108159, 2024.

Wille, J. D., Alexander, S. P., Amory, C., Baiman, R., Barthélemy, L., Bergstrom, D. M., Berne, A., Binder, H., Blanchet, J., Bozkurt, D., Bracegirdle, T. J., Casado, M., Choi, T., Clem, K. R., Codron, F., Datta, R., Di Battista, S., Favier, V., Francis, D., Fraser, A. D., Fourré, E., Garreaud, R. D., Genthon, C., Gorodetskaya, I. V., González-Herrero, S., Heinrich, V. J., Hubert, G., Joos, H., Kim, S.-J., King, J. C., Kittel, C., Landais, A., Lazzara, M., Leonard, G. H., Lieser, J. L., Maclennan, M., Mikolajczyk, D., Neff, P., Ollivier, I., Picard, G., Pohl, B., Ralph, F. M., Rowe, P., Schlosser, E., Shields, C. A., Smith, I. J., Sprenger, M., Trusel, L., Udy, D., Vance, T., Vignon, E., Walker, C., Wever, N., and Zou, X.: The extraordinary March 2022 east Antarctica "heat" wave. Part I: Observations and meteorological drivers, J. Clim., 37, 757–778, https://doi.org/10.1175/JCLI-D-23-0175.1, 2024.

Zhang, M., Yang, Y., Zhan, C., Zong, L., Gul, C., and Wang, M.: Tropical cyclone-related heatwave episodes in the Greater Bay Area, China: Synoptic patterns and urban-rural disparities, Weather Clim. Extrem., 44, 100 656, https://doi.org/10.1016/j.wace.2024.100656, 2024.

Zhang, X., Zhou, T., Zhang, W., Ren, L., Jiang, J., Hu, S., Zuo, M., Zhang, L., and Man, W.: Increased impact of heat domes on 2021-like heat extremes in North America under global warming, Nat. Commun., 14, 1690, https://doi.org/10.1038/s41467-023-37309-y, 2023.

Zhang, Y. and Boos, W. R.: An upper bound for extreme temperatures over midlatitude land, Proc. Natl. Acad. Sci. U.S.A., 120, e2215278 120, https://doi.org/10.1073/pnas.2215278120, 2023.

Zhang, Y., Held, I., and Fueglistaler, S.: Projections of tropical heat stress constrained by atmospheric dynamics, Nat. Geosci., 14, 133–137, https://doi.org/10.1038/s41561-021-00695-3, 2021.

Zschenderlein, P., Pfahl, S., Wernli, H., and Fink, A. H.: A Lagrangian analysis of upper-tropospheric anticyclones associated with heat waves in Europe, Weather Clim. Dynam., 1, 191–206, https://doi.org/10.5194/wcd-1-191-2020, 2020.